Search for right-handed currents in the decay chain of $K^+ \to \mu^+\nu_\mu$, $\mu^+ \to e^+\nu_e\bar{\nu}_\mu$

M. Aoki* and T. Yamazaki
Institute for Nuclear Study, University of Tokyo, Tanashi-shi, Tokyo 188, Japan

J. Imazato, Y. Kawashima,† K. H. Tanaka, and M. Takasaki
National Laboratory for High Energy Physics (KEK), Tsukuba-shi, Ibaraki-ken 305, Japan

R. S. Hayano, M. Iwasaki, H. Outa,‡ E. Takada,§ and H. Tamura
Department of Physics and Meson Science Laboratory, University of Tokyo, Bunkyo-ku, Tokyo 113, Japan
(Received 14 December 1993)

The asymmetry of positrons in the $K^+ \to \mu^+\nu$, $\mu^+ \to e^+\nu_e\bar{\nu}_\mu$ decay chain was measured in a search for right-handed weak currents in $\Delta S = 1$ semileptonic decay. High-intensity low-background monoenergetic polarized muons of 236 MeV/c momentum resulting from kaon decay at rest were directly extracted from a primary production target which was hit by a proton beam of the KEK 12-GeV proton synchrotron. Muons were stopped in a pure-aluminum plate, and the energy-integrated asymmetry of the decay positrons with respect to the incoming muon direction was determined to high precision. The observed asymmetry yielded $\xi P_\mu = -0.9996 \pm 0.0030(\text{stat}) \pm 0.0048(\text{syst})$. This result revealed no evidence of right-handed currents in this kaon-decay chain, and set a stringent bound on the mass of the right-handed weak boson.

PACS number(s): 13.20.Eb, 12.60.Cn, 13.35.Bv

I. INTRODUCTION

Experimental studies of the weak interaction are among today's most important subjects in particle physics. Many experiments have been performed since the discovery of parity violation [1–3], and the $V-A$ currents hypothesis [4] based on the famous experiment by Goldhaber *et al.* [5] is now almost an established fact, since no disproof of the $V-A$ hypothesis has yet been found in many experiments. However, on the other hand there is no reason to exclude right-handed $(V+A)$ currents from the theoretical framework from the beginning. It is also natural to believe that, although right-handed currents exist, they are suppressed for some reasons to such an extent that they are impossible to detect experimentally. Therefore, continuous efforts to improve the experimental sensitivity by using updated techniques are always of great interest and importance.

A number of experiments have been performed in leptonic and semileptomic processes such as β decay [6,7], muon decay [8–11], and neutrino deep inelastic scattering [12] in the search for right-handed currents. Nonleptonic cases of the K_L-K_S mass difference [13–16] and $B_d\overline{B}_d$ mixing [17,16] have been analyzed as well. Among these experiments, positron asymmetry measurements in the decay chain of $\pi^+ \to \mu^+\nu_\mu$, $\mu^+ \to e^+\nu_e\bar{\nu}_\mu$, and $K^+ \to \mu^+\nu_\mu$, $\mu^+ \to e^+\nu_e\bar{\nu}_\mu$ comprise one of the most powerful probes, unless the associated right-handed neutrino (ν_R) is heavy and decay is kinematically forbidden. The most precise data for the end-point positron asymmetry, which is equivalent to the muon polarization (P_μ) in conjunction with the muon decay Michel parameters (ξ, δ, and ρ [18]), was obtained as $|\xi P_\mu \delta/\rho| > 0.99682$ (90% C.L.) for the $\pi^+ \to \mu^+\nu_\mu$ $(\pi_{\mu 2})$, $\mu^+ \to e^+\nu_e\bar{\nu}_\mu$ decay chain at TRIUMF [9,10]. Another type of asymmetry measurement, the measurement of the energy-integrated positron asymmetry at PSI [11], derived $|\xi P_\mu| = 1.0027 \pm 0.0084$ for the π^+-μ^+-e^+ decay chain as well. Both quantities should be unity under the pure $V-A$ hypothesis, and are quite consistent with unity to high accuracy. For $K^+ \to \mu^+\nu_\mu$ $(K_{\mu 2})$ decay, an experiment was performed at KEK [19,20] nearly ten years ago, yielding $\xi P_\mu = -0.970 \pm 0.047$. The rather large error was dominated by a statistical error due to the smaller intensity of the available kaon beams, compared to that of the available pion beams.

Left-right symmetric (LRS) models [21,22] were proposed to explain the left handedness of the weak interaction by spontaneous symmetry breaking. In addition

*Present address: TRIUMF, 4004 Wesbrook Mall, Vancouver, B.C., Canada.
†Present address: Institute for Physical and Chemical Research, Wako-shi, Saitama 315-01, Japan.
‡Present address: Institute for Nuclear Study, University of Tokyo, Tokyo, Japan.
§Present address: National Institute of Radiological Sciences, Inage-ku, Chiba-shi, Chiba 263, Japan.

to the conventional weak boson (W_L), they assume another weak intermediate boson (W_R) which couples to the right-handed weak currents, replacing the standard gauge group $SU(2)_L \otimes U(1)$ with $SU(2)_L \otimes SU(2)_R \otimes U(1)$. In general, these weak bosons are a superposition of mass eigenstates ($W_{1,2}$), which can be written as $W_L = W_1 \cos\zeta + W_2 \sin\zeta$, $W_R = -W_1 \sin\zeta + W_2 \cos\zeta$, where ζ is the mixing angle. Then, the left handedness in the low-energy region can be attributed to $m_{W_2} \gg m_{W_1}$ and/or the smallness of ζ, where m_{W_i} is the mass of W_i. That is, right-handed phenomena in the low-energy region are suppressed by $\epsilon^2 = (m_{W_1}/m_{W_2})^4$. Regarding the coupling of W_R to a quark current, a right-handed Cabibbo angle (θ_R), which is an analogue to the ordinary Cabibbo angle (θ_L) [23], is also introduced. Although *manifest* LRS models [24] require that $\sin\theta_R = \sin\theta_L$, nonequality ($\sin\theta_R \neq \sin\theta_L$) can be postulated in general [25,26,16].

In the case of *manifest* left-right symmetry, there is no physical difference between the kaon- and the pion-decay positron-asymmetry experiments. However, if $\theta_R \neq \theta_L$ and $|\sin\theta_R| \simeq 1$, the kaon decay experiments are very sensitive to m_{W_2}, compared to that of the pion. The reason is that in kaon decay the hadron current couples to W_R with a vertex factor of $g\sin\theta_R$, but $g\cos\theta_R$ in pion decay. The deviation of $|\xi P_\mu|$ from unity can be expressed as

$$1 - |\xi P_\mu| \simeq 2\left(\epsilon\frac{\sin\theta_R}{\sin\theta_L} + \zeta\right)^2 + 2(\epsilon^2 + \zeta^2) \qquad (1.1)$$

for $K_{\mu 2}$ decay and

$$1 - |\xi P_\mu| \simeq 2\left(\epsilon\frac{\cos\theta_R}{\cos\theta_L} + \zeta\right)^2 + 2(\epsilon^2 + \zeta^2) \qquad (1.2)$$

for $\pi_{\mu 2}$ decay[1] [25,26]. This difference makes kaon decay much more sensitive to m_{W_2} than pion decay if $|\sin\theta_R|$ is large, as is shown in Fig. 1. Therefore, an improved experiment of the kaon decay with a similar statistical accuracy as the pion-decay experiment was designed to push up the mass limit.

In the present experiment we demonstrated that it is not necessary to have a high-intensity primary proton beam in order to increase the experimental sensitivity. We extracted a monoenergetic polarized muon beam of $K_{\mu 2}$ origin (p = 236 MeV/c) directly from a primary kaon production target with high intensity and low background, and stopped them in an aluminum stopping target for a precise measurement of the positron asymmetry. By this new method, the statistics was improved by 2 orders of magnitude compared to that of the previous kaon experiment at KEK [19,20]. An outline of the experiment and the results have already been reported briefly in Ref.

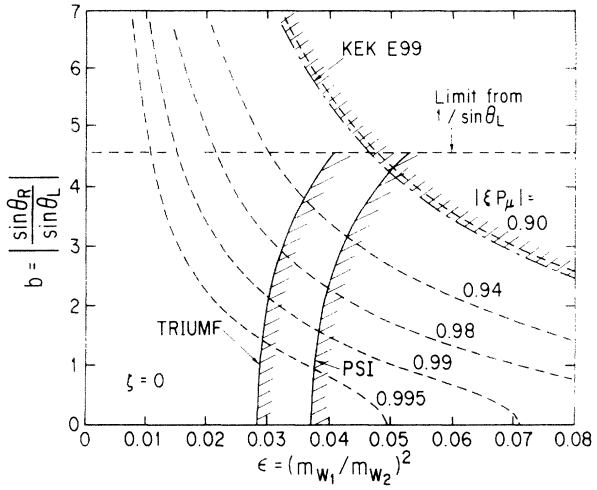

FIG. 1. 90% confidence limits on ϵ and $b = |\sin\theta_R/\sin\theta_L|$, where $\zeta = 0$ is assumed. The solid lines indicate the limits from $\pi_{\mu 2}$ decay experiments (TRIUMF [9,10] and PSI [11]). The dot-dashed lines are that from $K_{\mu 2}$ decay experiments (KEK [19,20]). The dashed lines indicate that the expected limits from $K_{\mu 2}$ decay experiment correspond to several $|\xi P_\mu|$ values.

[27]. In this paper we described the experiment in detail along with an analysis of the corrections and systematic errors worked out thoroughly.

II. EXPERIMENTAL METHOD

Since the kaon beam intensity is limited by the lower production cross section and the in-flight loss, it was difficult to gain statistics as high as that for pions by a "kaon beam line" method, which is usually used for kaon-decay experiments. We developed a new method which uses monoenergetic muons from $K_{\mu 2}$ decay at rest (hereafter called "$K_{\mu 2}$ muons") in the primary kaon production target, which preserves the initial polarization. By this method we succeeded in omitting the kaon extraction stage of the ordinary kaon decay experiment, and the event rate of kaon decay was increased drastically. That is just an analogue of a *surface muon* beam, which is the monoenergetic 29.8 MeV/c muon coming from the $\pi_{\mu 2}$ decay at rest near to the surface of a primary production target [28]. It is worth mentioning that such kinds of $K_{\mu 2}$ muons directly coming from a primary production target were reported by Abrosimov *et al.* [29] in the first.

A possible source of error in a $K_{\mu 2}$ muon beam experiment was contamination of muons coming from $\pi_{\mu 2}$ decay in flight. We thus constructed a dedicated beam line in order to reduce this background, and succeeded in reducing the contamination of $\pi_{\mu 2}$ muon to a level of a few percent. The influence of the still-remaining background could be corrected for and, thus, the systematic error resulting from background contamination was reduced to less than the 0.2% level.

In order to obtain the $\mu^+ \to e^+\nu_e\bar{\nu}_\mu$ decay asymme-

[1]Here we assumed the coupling constant of the right-handed sector g_R is equal to that of the left-handed sector g_L, and the *CP*-violating phases α and ω are zero [26].

try with low systematic error, we employed a muon-spin-rotation method under a transverse field (TFμSR) and measured the energy-integrated asymmetry (A) of the decay positrons. The advantages of this method are (1) the measured asymmetry is not affected by the different efficiencies of the positron counters, (2) high-energy resolution is not required, and (3) the ξ parameter in conjunction with the muon polarization can be determined as $\xi P_\mu = -3A$, which is independent of the other Michel parameters.

The muon decay time spectrum for an arbitrary muon polarization is expressed as

$$f(\theta, t) = N_0 e^{-\lambda t}[I(x) - \xi P_\mu C(x)\cos\theta], \qquad (2.1)$$

where N_0 is a normalization factor, λ the decay constant ($1/2.20\ \mu s^{-1}$), x the reduced electron energy ($x \equiv E_e/E_{\max}$) with $E_{\max} \equiv [m_\mu^2 - m_e^2]/2m_\mu = 52.8$ MeV, and θ the e^+ emission angle to the muon spin direction; further,

$$I(x) = 2[3(1-x) + 2\rho(4x/3 - 1)]x^2 \qquad (2.2a)$$

and

$$C(x) = 2[(1-x) + 2\delta(4x/3 - 1)]x^2\ . \qquad (2.2b)$$

Here, we assumed the four-fermion interaction theory, which is an applicable theory of the weak process in low-energy phenomena. In muon decay, the deviation in the four-fermion interaction from the intermediate vector boson exchange is of the order of $(m_\mu/m_W)^2 \simeq 10^{-6}$ [30]; it was negligible in the present experiment. The positron energy dependence of both $I(x)$ and $C(x)$ are shown in the upper part of Fig. 2. When the positrons with an energy greater than a threshold x_t are summed, the integral positron asymmetry becomes

$$A(x_t) = -\xi P_\mu \frac{\int_{x_t}^1 C(x)\,dx}{\int_{x_t}^1 I(x)\,dx}$$

$$= -\xi P_\mu \frac{1 - (3x_t^4 - 2x_t^3) - 8\bar{\delta}x_t^3(1-x_t)}{3 + (3x_t^4 - 6x_t^3) - 8\bar{\rho}x_t^3(1-x_t)}, \qquad (2.3)$$

where $\bar{\delta}$ and $\bar{\rho}$ are the reduced Michel parameters, and are $\bar{\delta} = 3/4 - \delta = 0.0014 \pm 0.0026(\text{stat}) \pm 0.0028(\text{syst})$ (90% C.L.) [31], $\bar{\rho} = 3/4 - \rho = -0.002 \pm 0.003$ (90% C.L.) [8], respectively. In the limit $x_t \to 0$, the uncertainty in $A(x_t)$ resulting from the finite errors of experimentally obtained $\bar{\delta}$ and $\bar{\rho}$ decreases rapidly with a factor of x_t^3, and becomes negligible.

Furthermore, since the energy-integrated asymmetry depends on the positron detection energy threshold, $E_{\min} \equiv x_t E_{\max}$, as is shown in the lower part of Fig. 2, we must minimize x_t as much as possible. A measurement of the integrated positron asymmetry with a lower energy threshold is essentially important for a precise experiment.

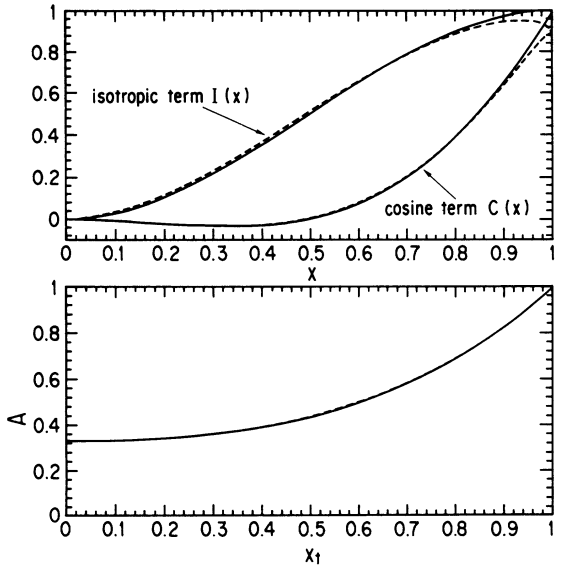

FIG. 2. Upper part shows the isotropic and cosine terms of the Michel spectrum as a function of the reduced energy ($x \equiv E/E_{\max}$). The lower part shows the integrated positron asymmetry [$A(x_t)$] as a function of an energy integration threshold of x_t. The solid curve indicates the calculated asymmetry assuming V–A currents. The dashed curve indicates the spectra with a radiative correction formulated by Kinoshita and Sirlin [40].

III. APPARATUS

This experiment was performed at the 12-GeV proton synchrotron at KEK. The plain view of the layout of the present experiment is shown in Fig. 3. A close-up view of the muon polarimeter part is also shown in Fig. 4. The newly designed beam line for the present experiment [32] transported $K_{\mu 2}$ muons with a total flux of 3500 per 10^{12} protons. The $K_{\mu 2}$ event rate was improved by 10^2 times compared to that in the previous kaon decay experiment [19,20].

The $K_{\mu 2}$ muons were degraded by a carbon block and were stopped in a muon stopping target. The spin of a muon rotates around a transverse magnetic field until it decays into e^+ with a lifetime of $\tau_\mu = 2.20\,\mu$s. The e^+ time spectrum at a positron detector placed perpendicular to the magnetic field showed a sinusoidal modulation superposed on the exponential decay curve. Two positron detectors were put on both sides of the μSR magnet in order to increase the number of events and to check the systematics of TFμSR data by comparing them. The attenuation of the positron decay asymmetry caused by the finite acceptance was corrected by means of positron tracking by drift chambers (EDCs). In addition, multiwire proportional chambers (MWPC1, MWPC2) and drift chambers (PDC, MDC) were placed in the beam axis in order to measure the initial direction of the muon, its scattering angle in the degrader and its stopping position.

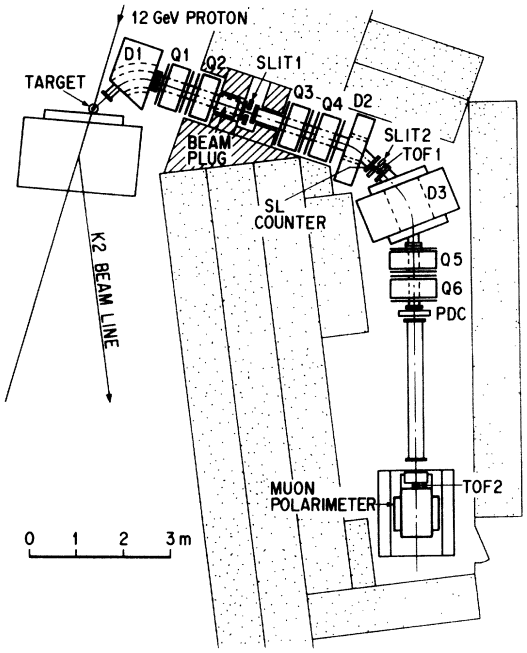

FIG. 3. Top view of the present experimental layout. There are two momentum slits (SLIT1,SLIT2) at two momentum dispersive focus points. SL counter was used as a second slit in order to avoid muon scattering on the surface of SLIT2. TOF1 and TOF2 are start and stop counters for TOF, respectively. PDC was a drift chamber to measure the beam profile at the Q6 exit.

A. Beam line

The present beam line was designed so as to obtain $K_{\mu 2}$ muons as much and as pure as possible. The background comes from in-flight $\pi_{\mu 2}$ decay with a continuous momentum spectrum. The design concept of the beam line was to increase the ratio of the $K_{\mu 2}$ muon to this continuous background, as well as the intensity. The concept was materialized as (i) backward extraction (147°), (ii) short distance to the first dipole magnet (D1) from the primary production target, (iii) high momentum resolution, and (iv) thin primary production target.

The pion production cross section with a 12-GeV incident proton has a peak in the forward angle, while the kaon stopped in the production target decays isotropically. Thus, backward extraction (i) reduced the pion contamination significantly. Furthermore, once the momentum is selected for a pion by D1 before its decay (ii), the in-flight decay muons from pions were mostly excluded at the second dispersive focus (SLIT2), since the decay muons have a different momentum. The optimum momentum width of $K_{\mu 2}$ muons is related to the thickness of the muon stopping target. In order to balance the systematical error resulting from positron interaction within the muon stopping target and the statistical error determined by the thickness of the kaon production target, an initial muon momentum broadening due to the energy loss in the kaon production target should be $\pm 0.5\%$ in dp/p (iv). Thus, the momentum bite of the present beam line was required to be $\pm 0.5\%$ (iii).

In order to reject pions, particle identification was performed according to the range difference and the time of flight (TOF). The range curves of π^+, μ^+, and e^+ are shown in Fig. 5, which were measured by changing the carbon block thickness. Since the carbon block thickness was set at the muon range so as to stop the muons at the muon stopping target, pions were mostly rejected. Then, a TOF measurement was carried out in order to reject the positrons as well as any residual pions which decayed in flight to muons in the carbon block and subsequently passed through it. A start counter (TOF1) was placed downstream of SLIT2 and a stop counter (TOF2) was placed 7 m downstream of TOF1. The TOF time spectrum after pion reduction by the carbon block is shown in Fig. 6. The contamination of pions was reduced to less than 0.02% by the TOF selection indexed in this figure.

The momentum spectrum of the beam line, measured

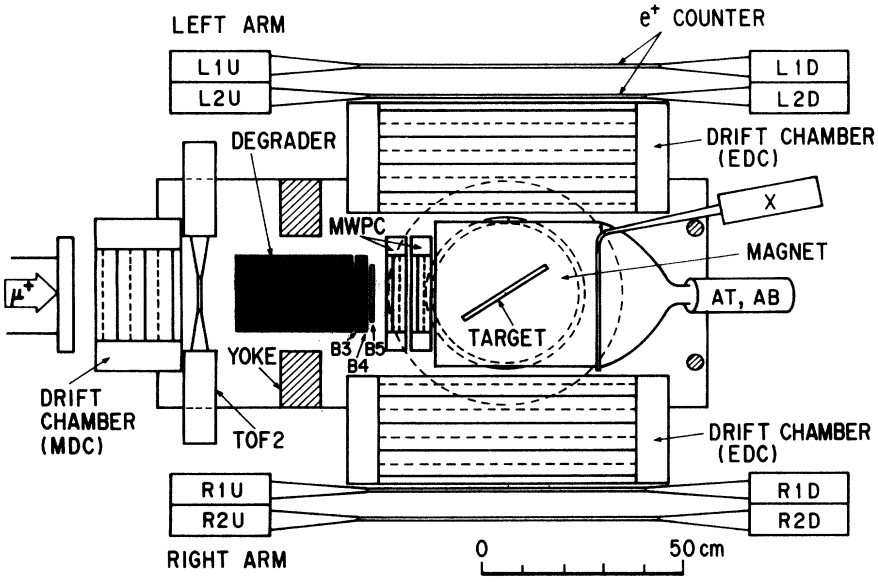

FIG. 4. Top view of the muon polarimeter apparatus. The magnetic field (105 G) at the target is vertical. $B3$, $B4$, and $B5$ are beam-defining counters. AT, AB, and X are veto counters, which are used for detecting muons stopped in the target. EDC's are drift chambers to measure positron emission angle. MDC is a drift chamber used to measure the flight direction of the incident muons. MWPC1/2 are multiwire proportional chambers to measure muon stopping position.

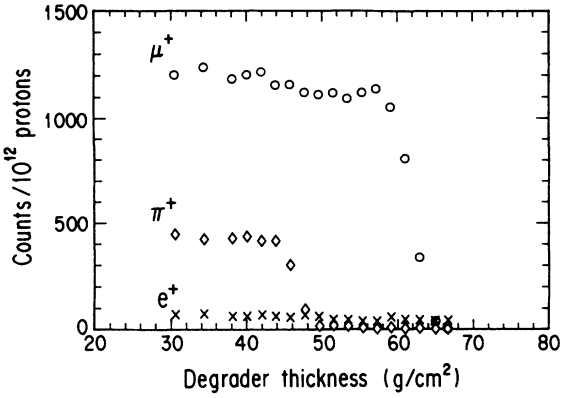

FIG. 5. Range curves of μ^+, π^+, and e^+ at MeV/c. They were measured by changing the carbon block ($\rho = 1.9$ g/cm^3) thickness. For the data taking, the thickness have been set at the edge of muon range curve.

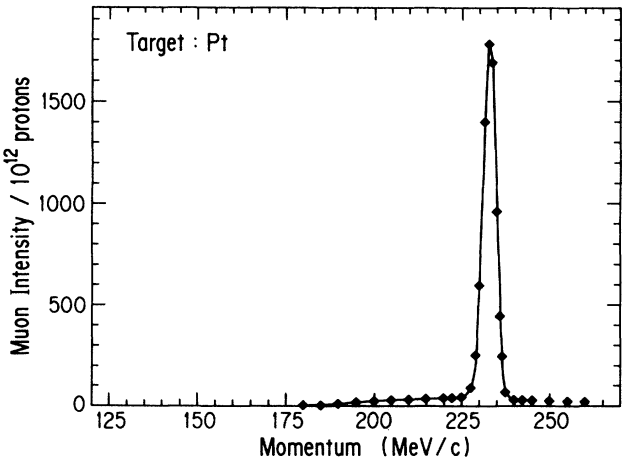

FIG. 7. Muon momentum spectrum with a 1.5-mm-thick Pt kaon-production target. The spectrum was measured by scanning the field strength of the beam line magnets. The flat component underlying the peak came from the decay in flight of pions.

by changing the channel momentum setting shown in Fig. 7, reveals a monoenergetic $K_{\mu 2}$-muon peak with a width of dp/p=2.0% [full width at half maximum (FWHM)], which is a superposition of the muon momentum width and the channel momentum bite. The muon intensity was 3500 per 10^{12} protons without TOF2 and 1800 per 10^{12} protons with TOF2; the peak-to-background ratio is 60. The continuous background came from the in-flight $\pi_{\mu 2}$ decay upstream of D1. This spectrum was obtained with a Pt target of 1.5 mm thickness, and a SLIT1 opening of ±5 mm. SLIT2 was opened to ±20 mm and a defining counter SL (0.8 cm×13 cm×0.2 cm^t) was placed at the center of the gap of SLIT2 so as to avoid muon scattering at the edges of SLIT2. For more details concerning the beam-line design see the reference by Tanaka *et al.* [32].

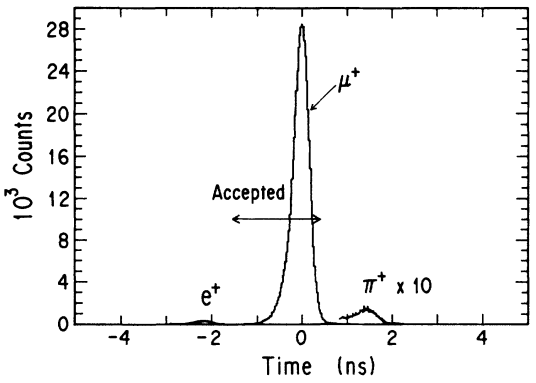

FIG. 6. TOF spectrum after pion rejection by a carbon block. The vertical scale of π^+ is 10 times the others. The events in the indexed region are accepted in the analysis.

B. Muon polarimeter

1. Muon tracking

Three types of tracking chambers were placed in the beam line: one was a drift chamber to measure the beam profile at the Q6 exit (PDC); the second was a drift chamber to measure the initial muon direction (MDC); the third was multiwire proportional chambers used to determine both the muon stopping position and the scattering angle in the degrader (MWPC1,2).

Since the incoming muons had a finite angular distribution of the flight direction, the muons were spuriously depolarized along the beam-line axis. In order to estimate this effect in a later analysis, we placed MDC upstream of TOF2. This chamber comprised 3 horizontal and 3 vertical layers, of which the drift length was 1 cm. The first layers of the horizontal and vertical planes were shifted by 1 cm, respectively, in order to solve the left-right ambiguity. The spatial and angular resolutions were 0.24 mm and 2 mrad, respectively. They were quite sufficient for our purpose.

In order to select muons that were surely stopped in the muon stopping target, tracking of muons downstream of the degrader was necessary. For this purpose, MWPC1 and MWPC2 with a wire spacing of 1 mm were placed near to the pole of the μSR magnet and separated by 72.5 mm from each other. The angular resolution was mainly restricted by multiple scattering in the chamber material, and was roughly estimated to be $\sim$ 0.01 rad.

With the help of these MWPC's the muon deflection angle was also measured in order to estimate the muon spin rotation via relativistic Coulomb scattering in the degrader block.

2. Muon degrader

A muon momentum degrader was placed downstream of TOF2. It was made of a set of carbon plates (20 cm × 20 cm, 1.9 g/cm^3); the total thickness was adjusted so as to obtain the maximum muon stopping rate in the target. This muon momentum degrader was also used for rejecting pions (as was already described).

As the momentum degrader, a light element material was required to minimize any muon depolarization due to Coulomb scattering with nuclei; that scattering is purely an electrostatic effect, but rotates the spin direction by a relativistic effect [33]. Since, the depolarization per unit length is roughly proportional to the square of the multiple scattering angle ($\delta P/dl \propto Z^2/A$) and the energy loss per unit length is $dE/dl \propto Z/A$, the depolarization per unit energy loss is roughly proportional to $\delta P/dl \times dl/dE \propto Z$. Thus, a light material was a better choice.

3. Muon stopping target

The most important feature of the muon stopping target is to minimize the depolarization of muons in the material. In general, depolarization is caused by (1) muonium formation, (2) any internal magnetic field, and (3) the magnetic dipole interaction with the surrounding nuclei. In order to avoid (1) and (2), a nonmagnetic metal is needed.

As for the first point, it is believed that there should be no muonium formation and, therefore, no loss of the initial polarization in a pure metal [34]. The spin relaxation effect in matter under a transverse magnetic field is parametrized by the relaxation rate (Λ), which is defined as $P_\mu(t) = P_\mu(0)e^{-\Lambda t}$. Then, the ideal material for the present experiment should have $\Lambda \simeq 0$. Grebinnik *et al.* [35] reported a small value of $\Lambda = 0.003 \pm 0.007\,\mu s^{-1}$ for "pure" aluminum at 290 K, which is interpreted as being the result of diffusional narrowing of the nuclear dipole interaction. They also reported a strong dependence of Λ on the impurities and temperature of the material. Therefore, aluminum of > 99.999% purity was used for the present experiment; it had been carefully annealed before so as to eliminate any lattice defects. Then, Λ was expected to be negligibly small.

The target had a size of 17 cm (height) × 22 cm (length) and a thickness of either 3 or 5 mm. It was placed in a magnet gap of 20 cm × 34 cmϕ tilted by 34° from the beam axis. The strength of the transverse magnetic field was chosen to be ~ 105 G in order to give a muon-spin-precession frequency of 1.43 MHz. A field map was measured by a hall probe with a 10^{-3} relative accuracy. The measured field distribution was used to calculate the damping function of the μSR precession pattern; this precision was sufficient for that purpose. The stability of the field strength was kept to within ±0.05% during the experiment.

The muon stopping target was surrounded by helium gas at normal pressure in order to minimize the muon stopping in the atmosphere. The spurious depolarization effect from the admixture of events stopped in the helium gas was estimated to be $\delta P = -0.0011$, and was corrected in a later analysis. The helium gas was contained in a thin plastic bag with a butyl rubber seal, which was put around the target holders.

4. Muon counters

Downstream of the degrader, three plastic scintillation counters ($B3$, $B4$, and $B5$) were placed for beam definition. Between $B3$ and $B4$ a carbon plate of 0.5 cm thickness was placed, and the energy losses of the incident particles in these counters were monitored so as to help in the particle identification. A μSR timer was started by the $B3$ signal. The muon momenta downstream of the degrader were distributed between 20 and 80 MeV/c; the muon spins were therefore rotated by different angles in the μSR magnetic field until stop in the target. If the μSR timer was started when a muon stopped in the target, this dispersion of the initial muon angle would provided spurious depolarization. Therefore, the μSR timer was started by $B3$ timing, which was placed outside of the magnetic field and at which the muon angles were not yet dispersed.

In order to identify any muons stopped in the target and to reject room background, three veto counters were placed around the target. One was placed downstream of the target (X); the other two were placed on the pole surfaces of the μSR magnet (AT,AB). The thresholds of these veto counters were set to be as low as possible.

5. Positron detector elements

In order to determine the emission angle of e^+ in the finite acceptance and to facilitate decay vertex reconstruction, the trajectory of each positron was traced by two drift chambers (EDC), which were symmetrically placed at the left and right arms. The positron detection system covered 50°–130° in the horizontal plane and ±10° in the vertical plane. Since a positron entered the EDC at such a large angle range, at least three layers were required in order to solve the left-right ambiguity of the drift chamber. In addition, a greater redundancy was needed in order to analyze the influence of the chamber inefficiency on the observed positron asymmetry (described in Sec. V B). The EDC comprised 4 horizontal and 4 vertical layers, the drift length being 2.5 cm. The last layer was shifted by 2.5 cm in order to solve the left-right ambiguity. The spatial and angular resolutions were 0.40 mm and 3 mrad, respectively, which were quite sufficient.

Two sets of trigger counters, each comprising two layers of plastic scintillators ($L1, L2$ and $R1, R2$), were placed behind the left- and right-side EDC, respectively. For each scintillator, photomultipliers were set on both the upstream (U) and downstream (D) sides. An e^+-hit-through signal was defined as the coincidence of two layers. The thicknesses of the first and second layers were 3 and 5 mm, respectively. The detection threshold energy was less than 1 MeV. The decay timing of the muon was defined as the mean of U and D photomultipliers timings, of which the resolution is about 1 ns, and was digitized

with a 10-ns time bin. The asymmetry distortion by such digitization was only $|\delta A| < 0.0001$.

6. *Trigger logic and data acquisition*

A muon stopped in the target was defined as

$$\mu\text{stop} \equiv \text{TOF1 TOF2 SL B3 B4 B5} \times\overline{(AB + AT + X)},$$

and the signal of the outgoing positron was defined as

$$e^+\text{good} \equiv (L1UL1DL2UL2D + R1UR1DR2UR2D) \times\overline{(AT + AB + X + B3 + B4 + B5)}.$$

The μSR time to digital converter (TDC) was started when a μSR start was asserted, where

$$\mu\text{SR start} \equiv \text{flat top} \cdot \text{computer ready} \times\mu\text{stop} \cdot \overline{\mu\text{stop}^*},$$
$$\mu\text{SR stop} \equiv e^+\text{good}.$$

The flat top asserts itself while the proton beam is being extracted. The μstop* is a 20-μs-long gate signal triggered by μstop. It was applied in order to separate the current muon event from a prestopped muon event, which was a so-called prepileup event. The μSR TDC was stopped at the e^+good timing.

Since the number of bytes per event was $\sim$ 260, and the event rate was $\sim 140\,\text{s}^{-1}$, the system should acquire $\sim$ 40k bytes/s. A Starburst (CES), which is a PDP-11 compatible microprocessor with a large memory in one CAMAC standard module, was used so that the dead time was only $\sim 500\,\mu$s per event and the event acceptance ratio was about 90%. The event data stored in the Starburst were transferred into a micro Vax II during the beam interval, and were recorded on 8mmVCR tapes. These data scheme was managed by the EXP data-taking system [36]. In order to monitor the measurement environment, some data were also recorded, such as the temperature of the experimental area, the power voltage of the preamplifier, and the excitation current of the μSR magnet.

IV. DATA ANALYSIS

Measurements were carried out for several conditions of the beam momentum and muon-stopping-target thickness, as shown in Table I. By comparing run 1 and run 2, in which the targets had different thicknesses, the effect of the positron scattering in the muon stopping target was studied and checked. In regard to the effect of the positron detection energy threshold, absorbers made of 1-cm-thick aluminum plate were inserted between $L1$ and $L2$, as well as $R1$ and $R2$ in run 3, so as to increase the energy threshold up to 5 MeV; the consistency was also studied. For the other runs, the absorbers were removed and the positron detection energy threshold was estimated to be less than 1 MeV.

Since the contamination of muons from the in-flight decay of pions had to be corrected, the background asymmetries (A_{bg}) were measured at five points, that is, at three lower momentum points and at two higher momentum points. The asymmetry of the background underlying at the $K_{\mu 2}$ peak was obtained by means of their interpolation. Details concerning this procedure are described in Sec. IV D. In order to check the validity of the background subtraction, off-peak runs of run 4 and run 5, of which the beam momentum were, respectively, set 1.8 MeV/c higher and lower than the $K_{\mu 2}$ peak, were performed.

An analysis was carried out so as to produce μSR precession time spectra with the possibly smallest background contamination and without any distortion. Any event selection on the data with EDC tracking would potentially bias the positron asymmetry, since it gives preference to the positron energy. Thus, we did not use the EDC tracking information for event selection as much as possible. After the analysis, the corrected precession time (t_{cor}) was calculated from the decay time (t) and the e^+ emission angle (ϕ) in the precession plane, with the expression

TABLE I. Run conditions. The beam-line momentum was slightly lower than the $K_{\mu 2}$ peak momentum (236 MeV/c), because of muon energy loss in the kaon production target.

Run No.	Beam momentum (MeV/c)	Degrader thickness (g/cm^2)	Target	Recorded events
1	233.0	60.0	3 mm thick	6.8×10^6
2	233.0	60.0	5 mm thick	8.5×10^6
3	233.0	60.0	5 mm with absorber	5.0×10^6
4	231.2	59.3	3 mm thick	4.8×10^6
5	234.8	61.2	3 mm thick	6.2×10^6
Background	214.5	50.7	5 mm thick	6.6×10^4
	219.7	53.2	5 mm thick	7.3×10^4
	224.9	56.2	5 mm thick	7.4×10^4
	240.6	63.6	5 mm thick	3.9×10^4
	245.9	65.4	5 mm thick	5.2×10^4

$$t_{\rm cor} = t - \frac{\phi}{\omega_0}, \quad \omega_0 = 9.05\,\mu{\rm s}^{-1}\,, \tag{4.1}$$

where ω_0 is the angular velocity of the muon spin precession at the central field (B_0). Then, the $t_{\rm cor}$ spectra were fitted to the function

$$f(t_{\rm cor}) = N_0 \exp\left(-\frac{t_{\rm cor}}{\tau}\right) \times\{1 + G(t_{\rm cor}) A \cos(\omega t_{\rm cor} + \phi_0)\} + {\rm bg}, \tag{4.2}$$

where N_0 is a normalization factor, τ is the muon lifetime, ω the muon spin precession angular velocity, ϕ_0 the initial phase of the precession, bg a constant background underlying the exponential decay spectrum, A the positron decay asymmetry, and $G(t_{\rm cor})$ a calculated damping function.

A. Muon analysis

The distribution of the incident angle of μ^+ had widths of 0.018 rad (FWHM) and 0.024 rad (FWHM) for the horizontal and vertical directions, respectively. Since this angular distribution is sufficiently narrow, although the muon incident angle was not corrected event by event, the muon-polarization attenuation due to this angular distribution, $\delta P = -0.0001$ was corrected later.

There were non-negligible amounts of muons which were stopped in the gas seal at around the target holders, which were made of butyl rubber; these muons might be more depolarized than those stopped in the target. Thus, we should eliminate any events from the muons stopped in the butyl rubber. Since we could not use the EDC tracking for this purpose (it would cause a positron asymmetry distortion), the μ^+ stopping position was obtained by taking the cross point of the μ^+ track and the muon stopping target plane. The distributions of the μ^+ stopping position along the vertical axis with and without a muon stopping target are shown in Fig. 8. For the empty-target condition, μ^+ stopped in the butyl rubber are seen as two prominent peaks in Fig. 8. The asymmetry from these peaks was experimentally determined to be $A_{\rm butyl} = 0.20 \pm 0.06$. We decided to accept $-60\,{\rm mm} < Y < 50\,{\rm mm}$ as stopped μ^+ in the target. With this cut, the butyl rubber event admixture was to an extent of 0.23%. Thus, the asymmetry distortion due to the contamination of butyl rubber event was estimated to be $\delta A = -[1/3 - (0.20 \pm 0.06)] \times 0.0023 = -0.0003 \pm 0.0001$.

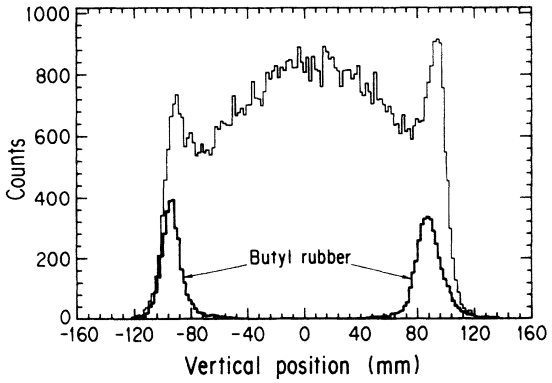

FIG. 8. Muon stopping height distribution measured by MWPC1 and MWPC2. The bold histogram is from empty-target run, while the thin histograms are from normal run.

B. Positron analysis

1. *Track fitting*

The hit positions on each layer of EDC were fitted to a straight line. In order to check the tracking quality and to reject any bad events, the fitting residue (χ^2) was calculated using

$$\chi^2 = \sum_i (X_i - x_i)^2,$$

where X_i is the real hit position and x_i is the fitted hit position on the ith layer, respectively. The χ^2 distribution has a long tail toward the large χ^2 region, as shown in Fig. 9. This tail was caused by multiple scattering of low-energy positrons. Therefore, event selection according to a cut on the χ^2 distribution affected the energy spectrum and biased the observed energy-integrated positron asymmetry. The energy response functions for several χ^2 cut parameters were calculated under the assumption of realistic chamber geometry and gas, and are shown in Fig. 10. From this figure it is obvious that a strict χ^2 cut eliminates mostly lower energy positrons and, thus, deforms the response function. Since a flat response function was needed, an event selection with a strict cut should be avoided. Furthermore, in the case of strict cutting the response function greatly changes when the cut parameter varies, so that the associated systematic error is larger. Therefore, the cut point should be at a large χ^2; a noncut would be the best choice if there

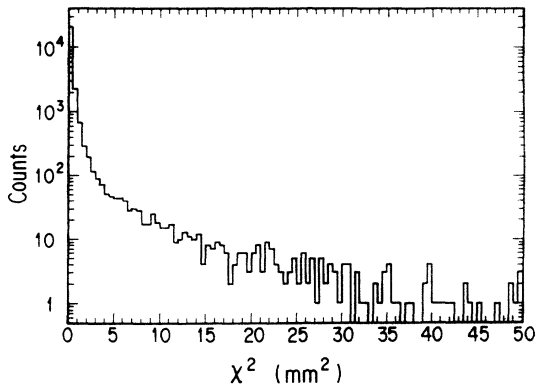

FIG. 9. Typical χ^2 distribution of EDC tracking. The tail component mainly stems from low energy positrons.

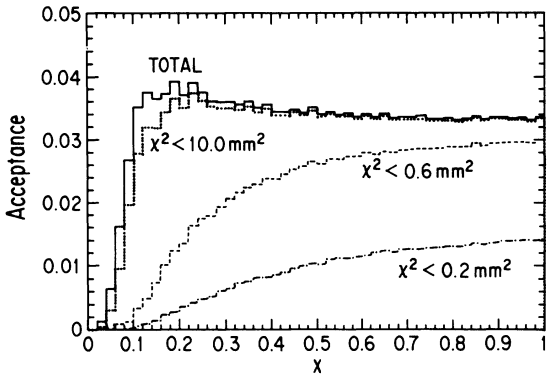

FIG. 10. Simulated response functions for several cases of χ^2 selection as a function of the reduced positron energy x ($\equiv E/E_{\max}$). It shows that a selection with small χ^2 mostly eliminates low-energy events and, furthermore, that the response function changes rapidly in small χ^2 region.

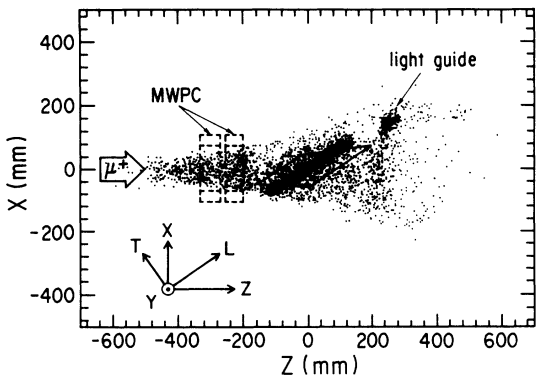

FIG. 11. Horizontal projection of reconstructed muon decay points. An event selection on Y ($-60\,\text{mm} < Y < 50\,\text{mm}$) was already carried out in this figure. The thickest image is of the muon stopping target and the flattened-square around it is a fiducial volume. The definition of axes are also shown.

were no contamination of garbage events. However, we decided to accept $\chi^2 < 10\,\text{mm}^2$ as being a reasonable choice, and estimated the effect of rejected events, as described into following.

The uncertainty of the asymmetry due to this ambiguity of the χ^2 cut is caused by two reasons. First, if a much looser cut would be taken, such as $\chi^2 < 200\,\text{mm}^2$, to save largely scattered events, the asymmetry would be changed by $\delta A = \pm 0.0003$, as was estimated by selecting the events in $10\,\text{mm}^2 < \chi^2 < 200\,\text{mm}^2$ of the experimental data. Regarding the $\chi^2 > 200\,\text{mm}^2$ region, it was revealed in a simulation that the fraction of events in this region was only 0.0001 of the total. It changes the asymmetry by only $\delta A \simeq 0.00001$, because the asymmetry in the $\chi^2 > 200\,\text{mm}^2$ region is evaluated to be 0.3 ± 0.1 by extrapolating the experimentally obtained asymmetry in the $\chi^2 < 200\,\text{mm}^2$ region. Thus, by neglecting the contribution from the $\chi^2 > 200\,\text{mm}^2$ region we assigned ± 0.0003 to the asymmetry uncertainty.

Second, if we assume that the $10\,\text{mm}^2 < \chi^2 < 200\,\text{mm}^2$ region is caused mostly by spurious signals, and that such signals also affect the small-χ^2 region, it changes the asymmetry by $\delta A = +0.0003$. Since that assumption is just a potential possibility of the asymmetry distortion, a systematic error $\delta A = \pm 0.0003$ was assigned to the asymmetry.

In addition, the positron asymmetry would be reduced by any angular resolution deterioration caused by a looser cut. The spatial resolution corresponding to the $\chi^2 < 10\,\text{mm}^2$ cut is $\delta x = \sqrt{\chi^2} \simeq 3\,\text{mm}$ at most. Since this spatial resolution gives an angular resolution attenuation of $\delta\theta \simeq 0.017$, $\delta A \simeq 0.0001$ at most. From a more precise estimation, in which we took an average of $\delta\theta$ with the weight of the χ^2 distribution, we obtained $\delta A < 0.5 \times 10^{-5}$; it is negligible.

After all, the uncertainty due to the χ^2 cut is estimated to be $\pm(0.0003 + 0.0003 + 0.5 \times 10^{-5}) = \pm 0.0006$, with taking a linear sum of these three uncertainties.

2. *Fiducial volume cut by the e^+ trajectory*

Here, we redefined the muon stopping position to be the cross point of a μ^+ trajectory and an e^+ trajectory. Fig. 11 shows the distribution of the thus-determined muon stopping positions in the horizontal plane. The flattened-square region in this figure shows the approximate fiducial region, that is $|T| < 50\,\text{mm}$ and $|L| < 100\,\text{mm}$ with T being the normal direction to the target plane and L being the horizontally long direction.

Along the vertical (Y) and L directions, we had already carried out event rejection with the μ^+ trajectory only. These rejections did not deform the energy spectrum from the Michel spectrum. Along the T direction, there was no alternative to define the μ^+ stopping position without using an e^+ trajectory. Consequently, this cut in T deforms the energy spectrum, resulting in a bias of the observed asymmetry, similarly to the χ^2 cut.

A typical μ^+ stopping position distribution along the T direction is shown in Fig. 12. In this figure, the fiducial

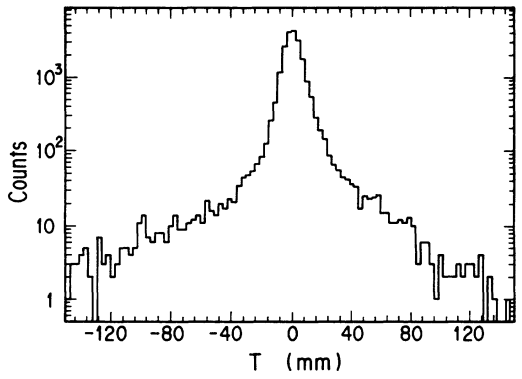

FIG. 12. Distribution of the reconstructed muon decay point along the T direction. L and Y cuts were already made. The tail mostly stems from low-energy positrons.

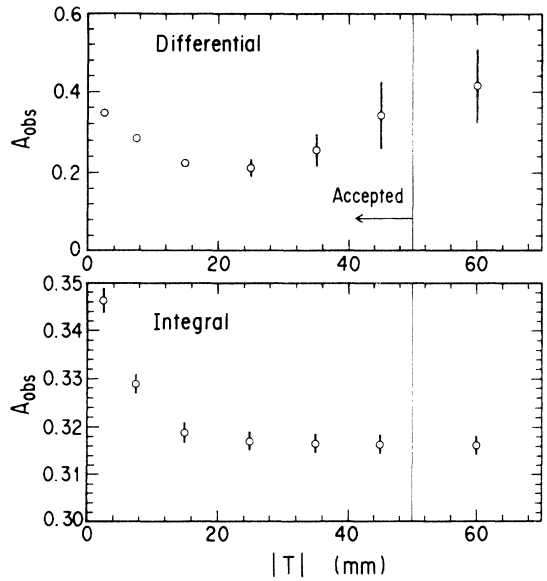

FIG. 13. T dependence of the positron asymmetry. The upper figure shows the differential contribution from each slice with $|T|$ and lower figure shows the integral dependence. The indexed region in the upper figure was accepted as good events.

cut along the L and Y directions using a μ^+ trajectory was already carried out. It is worth mentioning again that since a strict cut in T deforms the energy spectrum from the Michel spectrum, the best cutting point is infinitely large $|T|$, but only at the cost of background contamination. Thus, we decided to accept $|T| < 50$ mm, and regarded the eliminated events as coming from outside of the target.

Systematic errors originated from the ambiguity of this cut parameter and the evaluation of the background event contamination coming from outside of the target. In order to estimate these systematic errors, the differential and integral dependences of the experimentally obtained asymmetry on the T cut parameter were plotted, as shown in Fig. 13. First, if we assume that the events in the 50 mm $< |T| <$ 70 mm region, of which the asymmetry was found to be $A = 0.41 \pm 0.09$, resulted from background; these events thus also underlay in the relevant region, making an ambiguity of $\delta A = \pm 0.0003$. Second, if the cut parameter would be moved into the 30 mm $< |T| <$ 70 mm region (the region $|T| >$ 70 mm clearly touches with the image of MWPC and the light guide), δA would vary by ± 0.0004; thus, the uncertainty in the cut parameter gives $\delta A = \pm 0.0004$. After all, the error associated with the $|T|$ cut was estimated to be $\delta A = \pm(0.0003 + 0.0004) = \pm 0.0007$. Here again, for safety, we took a linear sum of these two errors.

C. Asymmetry fits

After eliminating bad events with the above-mentioned three cuts (Y, χ^2, T), the corrected precession time (t_{cor}) is calculated using Eq. (4.1). Typical t_{cor} spectra (run 1) of $B/B_0 > 0.9900$ are shown in Fig. 14, where B is the magnetic field strength at the muon stopped position and B_0 is the maximum field strength. The spectra of the other runs are quite similar. Then, the t_{cor} spectra were fitted to Eq. (4.2) with 6 free parameters (N_0, τ, ω, ϕ_0, bg, A) and 1 fixed function [$G(t_{cor})$] by means of a maximum-likelihood method using the MINUIT fitting program [37,38].

The asymmetry damping function [$G(t_{cor})$] was calculated from the magnetic field strength distribution, and was fixed during the asymmetry fit. Damping due to an interaction with the nucleus in the muon stopping target was not taken into account at all, since we used a pure-aluminum plate for the muon stopping target (as discussed in Sec. III B 3). The damping function was approximated by a quadratic function

$$G(t_{cor}) = 1 - \frac{t_{cor}^2}{\lambda^2} , \tag{4.3}$$

where λ characterizes the strength of the damping. In order to reduce the error caused by such a simple function approximation, the events were grouped into three field-strength regions: (a) $B/B_0 > 0.9994$, (b) $0.9950 < B/B_0 < 0.9994$, and (c) $0.9900 < B/B_0 < 0.9950$. The fitting was carried out for each of three field regions with different calculated λ's, which are given in Table II. The fitted-asymmetry uncertainty resulting from the quadratic function approximation of $G(t_{cor})$ is thus limited to $\delta A(\text{approx}) = \pm 0.00003$.

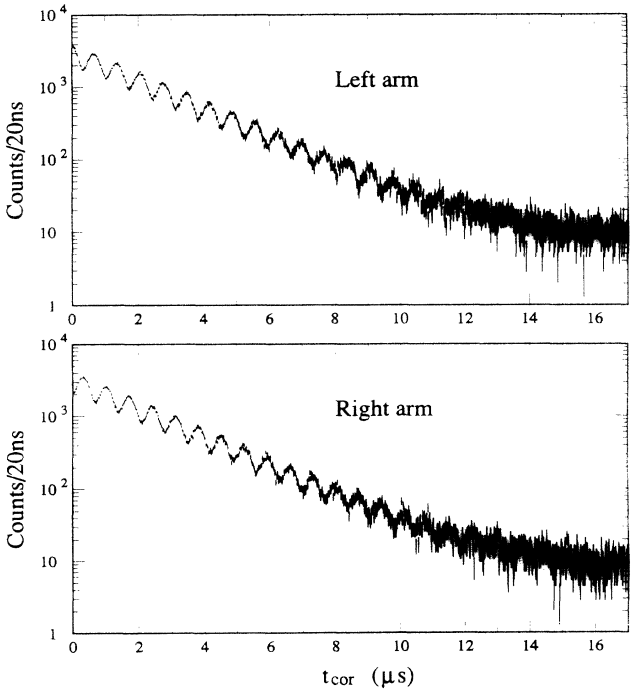

FIG. 14. Typical μSR time spectra (run 1). The upper part is of the left arm and the lower part is of the right arm. The emission angle on the precession plane has been corrected.

TABLE II. Event grouping on the field strength.

	B/B_0	$\lambda \times 10^2\ \mu$s		Percentage of
		left arm	right arm	events
a	> 0.9994	3.92	4.05	40%
b	0.9950–0.9994	0.836	0.887	43%
c	0.9900–0.9950	0.425	0.488	17%

The $G(t_{\rm cor})$ had other uncertainties, since it was calculated from the muon stopping distribution with the finite vertex resolution of the muon stopping point. The vertex resolution was mainly determined by multiple scattering of a muon in the MWPC. That effect was investigated using real data; it was revealed that the vertex resolution [σ_μ(rms)] was approximated by $\sigma_\mu^2 = 0.0014 \times (L - 250\,\text{mm})^2$, where L is the horizontal position of stopped muon along the muon stopping target plane. The uncertainty of this expression was estimated to be less than $\sim 30\%$. That error caused an uncertainty of $\delta A(\text{res}) = \pm 0.00010$, which was sufficiently small.

The error resulting from the uncertainty in the muon stopping distribution was also checked by changing the distribution shape, and was confirmed not to exceed $\delta A(\text{stop}) = \pm 0.00017$ by an extreme comparison of the uniform and realistic distributions.

In total, the uncertainty of the damping function gave a systematic error of

$$\delta A = \sqrt{\delta A^2(\text{stop}) + \delta A^2(\text{res}) + \delta A^2(\text{approx})}$$

$$= \pm 0.0002.$$

Finally, the asymmetry attenuation caused by the finite vertical acceptance of e^+ detection was corrected for by using the positron vertical angle distribution, which had 0.4 rad FWHM. The fitted asymmetries of left and right arms in three field-strength regions were then summed over with the weights of the number of events to obtain the observed asymmetries ($A_{\rm obs}$). They are listed in Table III with the reduced χ^2 of the fitting. The goodness of these χ^2 justified the assumption of the fitting function.

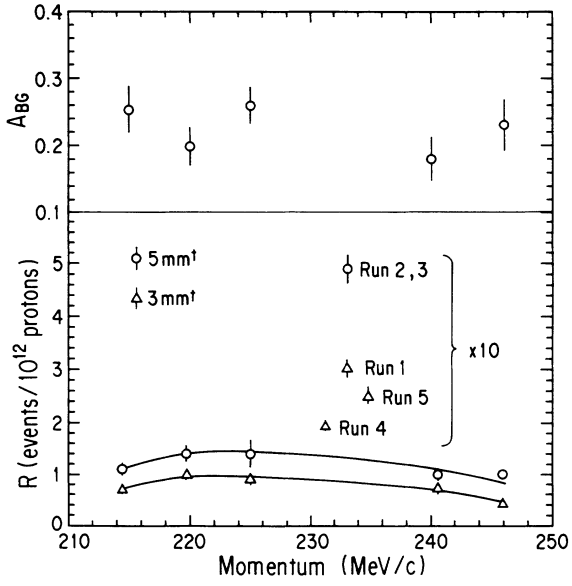

FIG. 15. Upper part shows background asymmetries and the lower part shows the event rates (R). In the lower part the circles are of a 5-mm-thick target and the triangles are of a 3-mm-thick target. The curves were drawn to join the points smoothly.

D. Analysis of π^+ in-flight-decay background

Since the $K_{\mu 2}$-muon beam was contaminated by muons from the in-flight decay of pions, the observed asymmetry would be shifted by

$$-\delta A_{\rm bg} = -\frac{R_{\rm bg}}{R_{\rm peak}}(A_{K_{\mu 2}} - A_{\rm bg})\ , \tag{4.4}$$

where $A_{K_{\mu 2}}$ is the positron asymmetry of $K_{\mu 2}$ muons, $A_{\rm bg}$ that of background, $R_{\rm bg}$ the background event rate, and $R_{\rm peak}$ that of $K_{\mu 2}$ peak. In order to correct for this effect, μSR precession patterns were measured at five background points, three lower momentum points and two higher momentum points.

In order to increase the statistics per one bin, the positron asymmetries of these points were analyzed using the same method, except for the following two points: (1) the events were not divided into three field-strength

TABLE III. Fitted asymmetries of five Runs. The reduced χ^2's of fitting (left arm/right arm) in regions a, b, and c are also listed, respectively.

Run No.	Momentum (MeV/c)	Target	No. of events survived	$A_{\rm obs}$	Reduced χ^2 of the fitting a	b	c
1	233.0	3 mm thick	380k	0.3235 ± 0.0025	1.043/1.001	0.999/0.999	0.995/1.005
2	233.0	5 mm thick	740k	0.3143 ± 0.0018	0.999/1.013	0.993/1.009	1.040/0.980
3	233.0	5 mm with absorber	680k	0.3344 ± 0.0019	1.085/1.083	1.047/1.163	0.997/1.032
4	231.2	3 mm thick	228k	0.3242 ± 0.0033	1.034/1.000	1.044/1.073	1.072/1.126
5	234.8	3 mm thick	302k	0.3176 ± 0.0029	1.046/1.004	1.018/1.061	1.058/1.019

TABLE IV. Event rates (R) per 10^{12} protons. The last column is the background correction to each Run.

Run No.	Momentum (MeV/c)	Target	R per 10^{12} protons	$\delta A_{\rm bg}$
Background		3 mm thick	0.9 ± 0.1	
		5 mm thick	1.3 ± 0.2	
1	233.0	3 mm thick	30.2 ± 0.5	$+0.0033 \pm 0.0006$
2,3	233.0	5 mm thick	49.0 ± 0.7	$+0.0029 \pm 0.0006$
4	231.2	3 mm thick	19.3 ± 0.2	$+0.0052 \pm 0.0009$
5	234.8	3 mm thick	25.1 ± 0.6	$+0.0040 \pm 0.0007$

regions and (2) they were dealt with using 40 ns binning. The asymmetry attenuation effect by such large binning is $\delta A = -0.0018$, much smaller than the statistical error of the background asymmetry ($\delta A \simeq \pm 0.015$). This statistical error is also larger than any other systematic errors by an order of magnitude. Thus, any corrections applied for normal runs were ignored.

The obtained precession spectra have the same phases as that of the $K_{\mu 2}$-peak spectra. It was therefore concluded that background muons presumably came from forward in-flight decay. The background asymmetries were obtained by fitting to Eq. (4.2) with the overall damping parameter, $\lambda = 0.503 \times 10^2\ \mu$s, which was also calculated from the magnetic field-strength distribution. The fitting results of five background runs are shown in the upper part of Fig. 15. They were consistent with each other, and were averaged to $\langle A_{\rm bg} \rangle = 0.222 \pm 0.015$.

The ratio of the background event rate to the peak event rate is naively expected to be 1/60 based on the muon momentum spectrum. However, the event rate was changed by the muon stopping target thickness, in general, since the muon stopping density was not uniform along the target thickness. The rates were evaluated for the 3 and 5 mm target thicknesses separately. The event rate (R) was defined as

$$R = R_T(N_L + N_R)/N, \tag{4.5}$$

where R_T is the trigger rate, N_L and N_R are, respectively, the number of left- and right-arm events surviving analysis, and N is the number of analyzed events. R is thus proportional to the total number of events in the finally obtained μSR spectrum with the normalization to the unit proton beam. The experimental values of R are shown in the lower part of Fig. 15 for the 3 and 5 mm thick targets. By fitting the circles (triangles) to arbitrary smooth curves, $R_{\rm bg}$'s were obtained, as is shown in Table IV. $R_{\rm peak}$'s were also obtained using the same analysis, and are also listed in Table IV. Finally, the asymmetry attenuation due to background contamination was derived by Eq. (4.4); the corrections to that attenuation ($\delta A_{\rm bg}$) are also listed in Table IV.

V. CORRECTIONS AND SYSTEMATICS

A. Positron scattering

The effect of positron scattering in the muon stopping target was estimated by using EGS4 [39], an electromagnetic shower simulation code developed at SLAC. EGS4 deals with the following seven interactions for e^+, e^-, and γ: (i) multiple scattering by nuclei, (ii) Bhabha and Møller scattering, (iii) bremsstrahlung and electron-positron pair production, (iv) the photoelectric effect, (v) Compton scattering, (vi) two-photon positron-electron annihilation, and (vii) Rayleigh scattering. Realistic geometries of the target, the veto counters, the positron counters, and the EDC were implemented into the simulation code. A magnetic field was also applied, and muon-decay events were generated by assuming the Michel spectrum with the radiative corrections formulated by Kinoshita and Sirlin [40]. The simulated positron asymmetries ($A_{\rm sim}$) based on the three conditions (the 3 mm thick target, the 5 mm thick target, and one with an absorber) are listed in Table V in terms of $\delta A_{\rm sim} \equiv \frac{1}{3} - A_{\rm sim}$. The errors resulted from the statistics of the simulation.

From the simulation study it was found that $\delta A_{\rm sim}$ mainly consisted of the following three contributions: (i) positron multiple scattering, (ii) knock-on electron veto, and (iii) knock-on electron trigger.

For multiple scattering, the most crucial effect was contamination of large-angle scattered positrons. Even if the initial direction of the emitted positron was not aimed at the positron detector, the flight direction was drastically changed via large-angle multiple scattering to enter the positron detector. This effect effectively changed the acceptance of lower energy positrons by the energy dependence of the scattering cross section. This fact was experimentally verified by run 3. That is, since the energy of such scattered particles was low and they were easily rejected by the absorber, the observed asymmetry of run 3 is not so much shifted from 1/3.

The events rejected by a knock-on electron hitting the veto counter were 4% of the normal events. Since the cross section of the knock-on process is proportional to $1/E^2$, low-energy positrons tend to be rejected. There-

TABLE V. Simulated positron asymmetries ($A_{\rm sim}$) and corrections to $A_{\rm obs}$, $\delta A_{\rm sim} \equiv 1/3 - A_{\rm sim}$. The errors resulted from the simulation statistics.

Target	$A_{\rm sim}$	$\delta A_{\rm sim}$
3 mm thick	0.3257 ± 0.0013	$+0.0076 \pm 0.0013$
5 mm thick	0.3201 ± 0.0010	$+0.0132 \pm 0.0010$
5 mm with absorber	0.3390 ± 0.0011	-0.0057 ± 0.0011

fore, the asymmetry of the rejected events must be less than 1/3. Actually, $A \simeq 0.22$ was obtained based on a simulation of the rejected events. This effect increases the observed asymmetry ($A_{\rm obs}$) by ~ 0.005.

Furthermore, the events triggered by a knock-on electron instead of a primary positron were also involved to the extent of 4%. The asymmetry of such events was estimated to be $\simeq 0.22$ from the simulation. Since these events could not be distinguished from the normal positron-triggered events in the present setup, this effect attenuates the observed asymmetry by ~ 0.005.

Not only these three effects, but also the other effects resulting from the minor interactions (for example, two-photon positron-electron annihilation), were mutually correlated with each other. Since it is impossible to estimate them separately, an overall simulation was performed. The uncertainty in the Monte Carlo simulation resulted from the cutoff parameters of the EGS4 code as well as the statistics of the simulation. It produced an uncertainty of the asymmetry, $|\delta A| < 0.00073$. It is not so small, and is one of the main sources of systematic error in the present experiment. More details concerning the simulation of e^+ interaction and its uncertainty are given in Appendix B.

B. EDC inefficiency

Since the detection inefficiency of the EDC might be larger for higher energy e^+, it may distort the observed energy-integrated positron asymmetry. The averaged detection inefficiency of the EDC was measured to be $\varepsilon = 0.014 \pm 0.002$ per one layer. Thus, the percentage of events with more than 3 no-hit layers was on the order of $\varepsilon^4 \simeq 10^{-8}$, which is clearly negligible. On the other hand, the percentage of 3-no-hit-layer events was $48 \times \varepsilon^3 \simeq 0.00015$, where 48 resulted from the number of combinations of 4 vertical and 4 horizontal layers of EDC. It was impossible to obtain the asymmetry of these events from the present setup. Since the asymmetry must be between $-1/3$ and 1 from Eq. (2.2), we decided to assign $|\delta A| < 0.00015$ to the systematic error.

In regard to the 0-, 1-, or 2-no-hit-layer events, they were analyzed simultaneously in a normal analysis, except for 2-hit-horizontal-layer and 2-hit-vertical-layer events. It was impossible to solve the left-right ambiguity from only two layers. Therefore, a trigger counter analysis, which did not use the EDC tracking data, were performed. The amplitude of μSR time spectrum was then attenuated by the finite-angle acceptance of positron detection and garbage event contamination. Their effect was estimated by comparing the asymmetry of the good events in a normal analysis and in this counter analysis. Then, the asymmetry of such two-layer events was obtained to be 0.153 ± 0.065, so that the observed asymmetry had to be corrected with $-12 \times \varepsilon^2 \times (\frac{1}{3} - 0.153 \pm 0.065) = -0.0004 \pm 0.00015$. The total correction and the error to the observed asymmetry due to the EDC inefficiency was then concluded to be $\delta A = -0.0004 \pm 0.0003$.

C. Muons-in-gas contamination

The fiducial volume cut was made loose along the T direction in order to avoid any asymmetry distortion which was caused by a positron energy preference. We accepted $|T| < 50$ mm while the target thickness was 5 mm (3 mm); 0.13% (0.22%) of the muons was stopped in helium gas around the muon stopping target. The positron asymmetry of the muon stopped in the helium gas is known to be $A_{\rm He} = 0.10$ for 1.2 atm [41] with some pressure dependence. A correction $\delta A = 0.00038 \pm 0.00038$ was adopted by taking weighted mean values of 0.13% and 0.22%.

D. Muon spin rotation by Coulomb scattering

In general, a charged particle passing through an electrostatic field can also feel a magnetic field induced by a Lorentz transformation of the electrostatic field. Thus, the spin of the particle rotates, even if the scattering occurs due to a pure Coulomb interaction. The depolarization along the initial momentum direction ($\eta_{\parallel}^i$) of particles traveling through thin matter is formulated to be [33]

$$\eta_{\parallel}^i = \frac{1}{2}\left[\frac{1}{2}(g-2)\frac{\gamma^2-1}{\gamma} + \frac{\gamma-1}{\gamma}\right]^2 \left(\frac{M_S}{\beta p}\right)^2 \frac{\Delta l}{L_R}, \quad (5.1)$$

where g is the gyromagnetic factor, $\gamma = (1-\beta^2)^{-1/2}$ with β being the velocity of the particles, $M_S = 19.2\,\mathrm{MeV/c}$, L_R is the radiation length of material, and Δl is the material thickness.

Equation (5.1) is approximated as

$$\eta_{\parallel}^i \simeq \frac{1}{2}\left(\frac{\gamma-1}{\gamma}\right)^2 \frac{M_S^2}{\beta^2 p^2}\frac{\Delta l}{L_R} = \frac{M_S^2}{2m_\mu^2}\frac{1}{(\gamma+1)^2}\frac{\Delta l}{L_R}. \quad (5.2)$$

Regarding the muon depolarization until being stopped in the muon stopping target with a range l, $\eta_{\parallel}^i$ lies in the region

$$\frac{M_S^2}{2m_\mu^2}\frac{1}{(\gamma_0+1)^2}\frac{l}{L_R} < \eta_{\parallel}^i < \frac{M_S^2}{2m_\mu^2}\frac{1}{2^2}\frac{l}{L_R}, \quad (5.3)$$

where $\gamma_0 \leq 1.38$ is the γ factor of a muon at the target entrance. Taking the average muon path length to be $\langle l \rangle = 4.6$ mm (run 2, 3), a limit was set as

$$0.00015 < \eta_{\parallel}^i < 0.00021.$$

We thus assigned 0.0002 ± 0.0001 to $\delta P_{\rm Al}$.

Next, the depolarization in the material upstream of MDC, such as the kaon production target, was considered. The depolarization along the final momentum direction ($\eta_{\parallel}^f$) must be adopted for them, since the incident angle of each muon was measured by MDC. A modification of the Eq. (5.1) gives

$$\eta_{\parallel}^{f} = \frac{1}{2}\left[\frac{1}{\gamma} - \frac{1}{2}(g-2)\frac{\gamma^2-1}{\gamma}\right]^2 \left(\frac{M_S}{\beta p}\right)^2 \frac{\Delta l}{L_R}. \quad (5.4)$$

Using this expression, the depolarization correction in the production target was calculated to be $\delta P = +0.0002$ (run 1,2,3), $\delta P = +0.0003$ (run 4), $\delta P = +0.0001$ (run 5). The differences came from a variety of averaged penetration depths of the muons in the production target. We therefore assigned a correction and a systematic error of $\delta P_{\rm Pt} = +0.0002 \pm 0.0001$ to the muon polarization. The depolarization caused by other materials, such as vacuum windows of beam ducts, the SL counter, TOF1/2 counters, and air gap, was also calculated to be 0.00004, and a correction of $\delta P_{\rm bm} = +0.00004$ was assigned.

In order to calculate the depolarization due to scattering in the degrader, the above expressions could not be used directly, since they are valid for only a thin material. Thus, a Monte Carlo simulation in which the degrader was divided into many thin slabs so as to make the above expressions applicable was performed. The simulated scattering-angle distribution of the muons is shown in Fig. 16 by a solid histogram together with the measured scattering-angle distribution (open circles). Both the calculated and measured scattering-angle distributions coincide well with each other, showing that the simulation was sufficiently valid and accurate for the present estimation. The resulting simulated spin rotation-angle distribution is also indicated in Fig. 16 by a dashed histogram. From this simulation, the correction and the systematic error for the degrader scattering was $\delta P_{\rm dg} = +0.0008 \pm 0.00007$, by averaging the cosine of the spin rotation angle. The error resulted from a difference between the data and the simulation.

Finally, the correction and error to the muon polarization due to multiple Coulomb scattering is estimated to be

$$\begin{aligned}\delta P_\mu &= \delta P_{\rm Pt} + \delta P_{\rm bm} + \delta P_{\rm dg} + \delta P_{\rm Al} \\ &= 0.0012 \pm 0.0002.\end{aligned}$$

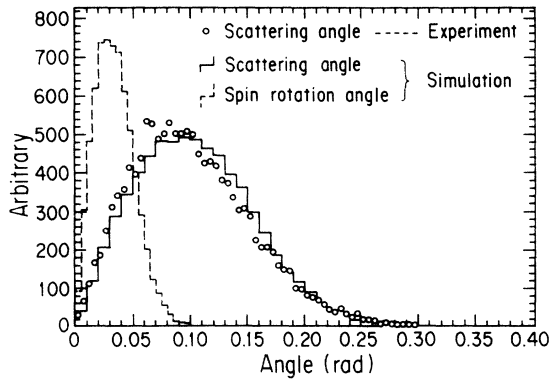

FIG. 16. Distribution of the muon scattering angle by the carbon degrader block. The solid histogram is of the simulated distribution and the circles are of measured distribution. The dashed histogram is the distribution of the simulated muon spin rotation angle by Eq. (5.1).

E. Scattering on the surface of the beam duct

During the transport of the beam, muons could be scattered at the inner surface of the beam duct and the surface of the slits. Such muons are depolarized more than straightly transported muons. The percentage of scattered muons was calculated using the code DECAY TURTLE [42]. This calculation reproduced the SLIT1 opening dependence of the muon yield and the muon profile measured by PDC at the Q6 exit. It justifies the accuracy of the beam transport calculation.

From that calculation, it turned out that muons scattered on the beam duct at Q5 were dominant; the percentage was estimated to be 30% at most. Since it is too complicated to treat the reflection of muons exactly, the worst case, in which all of these muons are reflected, was assumed in order to simplify the subsequent analysis. From a Monte Carlo simulation it was found that those muons with a momentum of $p > 215$ MeV/c could only arrive at the muon stopping target, while a muon with a momentum of $p < 215$ MeV/c would be stopped in the degrader. The maximum depolarization corresponding to $p > 215$ MeV/c was calculated according to a relation derived from Eq. (5.4):

$$\eta_{\parallel}^{f} = \frac{1}{2}\frac{1}{\gamma^2}\frac{M_S^2}{\beta^2 p^2}\left[\frac{\Delta E}{\Delta x}\right]^{-1}\frac{\Delta E}{L_R}, \quad (5.5)$$

to be $\eta_{\parallel}^{f} = 0.0009$. Thus, the averaged depolarization of muons transported to the muon stopping target was estimated to be $|\delta P_\mu| < 0.0009 \times 0.3 = 0.0003$, at most.

Although scattering also occurred in other parts of the beam line, the percentages of scattered muons were smaller and the depolarizations were estimated to be $|\delta P_\mu| < 0.00005$ upstream of SLIT1, $|\delta P_\mu| < 0.00002$ at SLIT1 and $|\delta P_\mu| < 1.3 \times 10^{-6}$ between SLIT1 and the SL counter.

In total, the muon depolarization uncertainty due to surface scattering was concluded to be $|\delta P| < 0.0004$.

F. Spin-exchange scattering with atomic electrons

Here, we discuss the effect of the muon spin flip due to spin-exchange scattering with unpolarized electrons in matter. Different from the nonrelativistic case of a surface muon coming from π^+ decay at rest [43,10,11], the $K_{\mu 2}$ muon requires an exact treatment of the spin-exchange scattering cross section. The averaged depolarization $\langle Q \rangle$ and energy loss $\langle \Delta T \rangle$ by a single scattering with an atomic electron were obtained by numerical integration:

$$\langle Q \rangle = \int_0^{2\pi}\int_{\theta_0}^{\pi}\left(2\frac{\sigma_S}{\sigma_T}\right)\sigma_T \, d\Omega \quad (5.6)$$

and

$$\langle \Delta T \rangle = \int_0^{2\pi}\int_{\theta_0}^{\pi} \Delta T \sigma_T \, d\Omega, \quad (5.7)$$

where σ_S is the spin-flip cross section and σ_T is the to-

tal cross section. Both diverge when θ_0 goes to zero. However, the ratio $\langle Q\rangle/\langle \Delta T\rangle$ converges because the functional profile becomes the same in the limit $\theta_0 \to 0$. Thus, we numerically calculated the ratio $\langle Q\rangle/\langle \Delta T\rangle$.

For the present calculation, θ_0 was set to a finite value of $\theta_0 \simeq 4 \times 10^{-6}$, corresponding to $T \simeq 1$ eV, since it is not conceivable that the atomic electron is free at a small θ_0 region, because the averaged ionization energy of carbon is 76 eV. The calculated $\langle Q\rangle/\langle \Delta T\rangle$ is shown in Fig. 17 with two cases of the polarization axis. For the solid curve the polarization axis is defined along the initial muon flight direction. For the dashed curve it is along the final muon flight direction. In the present case, the former definition was adopted.

Since the energy loss of a particle passing through matter is dominated by scattering with atomic electrons, the muon depolarization until the muon stops in the target is obtained by integrating $\langle Q\rangle/\langle \Delta T\rangle$ from the initial kinetic energy to zero. Thus, the correction and its error due to muon spin-exchange scattering with electrons is

$$\delta P = \int_0^{152.9\ \mathrm{MeV}} \frac{\langle Q\rangle}{\langle \Delta T\rangle}\, dT = 0.0008 \pm 0.0003.$$

The error comes from the uncertainty in the numerical integration.

The muon spin can also be flipped by spin-exchange scattering with nuclei. For example, it was found that depolarization by a spin-spin interaction with hydrogen nuclei in the scintillator is negligible. This fact can be easily understood by considering $\mu_P = \mu_e/658$, where μ_P and μ_e are the magnetic moments of a proton and an electron, respectively.

G. $K^+ \to \mu^+\nu_\mu\gamma$ decay contamination

An admixture of muons from the radiative decay $K^+ \to \mu^+\nu_\mu\gamma$ into $K_{\mu 2}$ muons slightly decrease the initial muon polarization. The radiative decay $K^+ \to \mu^+\nu_\mu\gamma$ comprises the following three terms: internal bremsstrahlung (IB), structure decay (SD), and interference between them (INT). The SD term is very ambiguous and includes interesting physics; many theoretical calculations involving its vector form factor (F_V) and the axial-vector form factor (F_A) have been carried out. However, since the theories strongly depend on models, the experimental limits [44], that is $|F_V + F_A|m_K < 0.23$ and $-2.5 < (F_V - F_A)m_K < 0.3$ with the m_K being the mass of a charged kaon, were employed for the present correction.

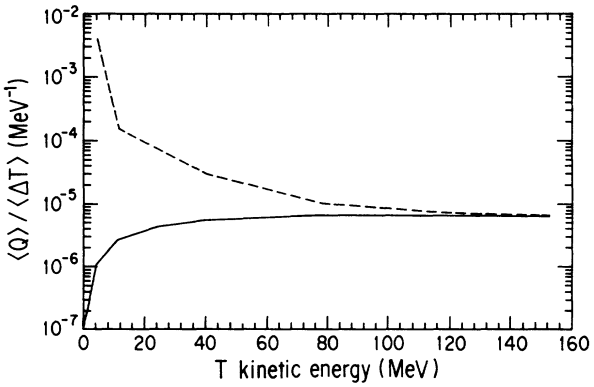

FIG. 17. Spin flip probability per unit energy loss in the material. For the solid curve the polarization axis is defined along the initial muon flight direction. For the dashed curve it is along the final muon flight direction.

The muon polarization of this radiative decay was formulated by Bardin and Bilenky [45] without using any models for the intermediate states on the SD term. The calculated muon polarization using their formula and the experimentally obtained form factors reveals that the muon polarization in the range 233 MeV/$c < p <$ 235.1 MeV/c becomes $\langle P_\mu\rangle = 0.9998$ by taking an average of the polarization with the weight of the decay probability. The lower limit of the muon momentum ($p >$233 MeV/c) came from the momentum acceptance of the present beam line. Since the decay probability diverges at the $p \to$235.5 MeV/c limit, it is impossible to calculate the exact value of the muon polarization. However, it is clear that the muon polarization should be at least $|P_\mu| > 0.9998$, and that the real value must be much closer to unity. Thus, we assigned a systematic error of $|\delta P| < 0.0002$ due to the admixture of the kaon radiative decay.

VI. RESULTS

We now combine the observed positron asymmetry (A_{obs}) with the corrections to obtain the final result. The corrections and the systematic errors are summarized in Tables VI and VII.

Regarding the correction to the positron asymmetry, both the correction and the associated error were dominated by the positron scattering process, which gave $\delta A = +0.0076 \pm 0.0013$ for run 1,4,5, $\delta A = +0.0132 \pm 0.0010$ for run 2, and $\delta A = -0.0057 \pm 0.0011$ for run 3. Futhermore, these corrections were accompanied by a simulation ambiguity, $\delta A = \pm 0.00073$. The contamination of muons coming from π^+ in-flight decay also gave considerable corrections, which were $\delta A = +0.0033 \pm 0.0006$ (run 1), $\delta A = +0.0030 \pm 0.0006$ (run 2,3), $\delta A = +0.0052 \pm 0.0009$ (run 4), and $\delta A = +0.0040 \pm 0.0007$ (run 5). The other corrections, such as the time binning, time origin, cut parameters, EDC efficiency, EDC mistracking, muons-in-gas events, and damping function, were combined to be $\delta A = +0.0005 \pm 0.0013$, the error of which was of the same magnitude as that of the positron scattering process.

For the correction and error to the muon polarization, muon scattering in the degrader (both Coulomb and spin-exchange process) gave a relatively large contribution to the correction. On the other hand, the error was dominated by an estimation of the muon scattering in the beam duct. The uncertainty resulting from the

TABLE VI. Corrections and associated systematic errors to the observed positron asymmetry. A subtotal in the last line was taken from the simulation ambiguity to the damping function.

Origin		δA
Positron scattering		
	Run 1,4,5	$+0.0076 \pm 0.0013$
	Run 2	$+0.0132 \pm 0.0010$
	Run 3	-0.0057 ± 0.0011
Background contamination		
	Run 1	$+0.0033 \pm 0.0006$
	Run 2,3	$+0.0030 \pm 0.0006$
	Run 4	$+0.0052 \pm 0.0009$
	Run 5	$+0.0040 \pm 0.0007$
Simulation ambiguity		± 0.00073
Time binning		$+0.0001$
Time origin		negligible
Cut parameters		
	Y	$+0.0003 \pm 0.0001$
	χ^2	± 0.0006
	T	± 0.0007
EDC efficiency		-0.0004 ± 0.0003
EDC mistracking		$+0.0001$
Muons-in-gas		$+0.0004 \pm 0.0004$
Damping function		
	Muon stopping distribution	± 0.00017
	Vertex resolution	± 0.0001
	Quadratic approximation	± 0.00003
	Field map	negligible
$\mu^+ \to e\nu_e\bar{\nu}_\mu\gamma$		included in the simulation
Subtotal		$+0.0005 \pm 0.0013$

TABLE VII. Corrections and associated systematic errors to the initial muon polarization.

Origin		δP
Coulomb scattering		
	Target	$+0.0002 \pm 0.0001$
	Beam line elements	$+0.00004$
	Degrader	$+0.0008 \pm 0.00007$
	Muon stopping target	$+0.0002 \pm 0.0001$
Spin exchange with atomic electrons		$+0.0008 \pm 0.0003$
Muon incident angle		$+0.0001$
Scattering in the beam duct		< 0.0004
$K^+ \to \mu^+\nu_\mu\gamma$		< 0.0002
Total		$+0.0021 \pm 0.0005$

TABLE VIII. Positron asymmetries and their corrections with final results of ξP_μ.

Run	A_{obs}(stat)	δA_{sim}(syst)	δA(syst)	δA_{bg}(syst)	δP(syst)	ξP_μ(stat)(syst)
1	0.3235(25)	0.0076(13)	0.0005(13)	0.0033(06)	0.0021(05)	−1.0068(75)(58)
2	0.3143(18)	0.0132(10)	0.0005(13)	0.0030(06)	0.0021(05)	−0.9951(54)(53)
3	0.3344(19)	−0.0057(11)	0.0005(13)	0.0030(06)	0.0021(05)	−0.9984(57)(54)
4	0.3242(33)	0.0076(13)	0.0005(13)	0.0052(09)	0.0021(05)	−1.0146(99)(62)
5	0.3176(29)	0.0076(13)	0.0005(13)	0.0040(07)	0.0021(05)	−0.9912(87)(59)

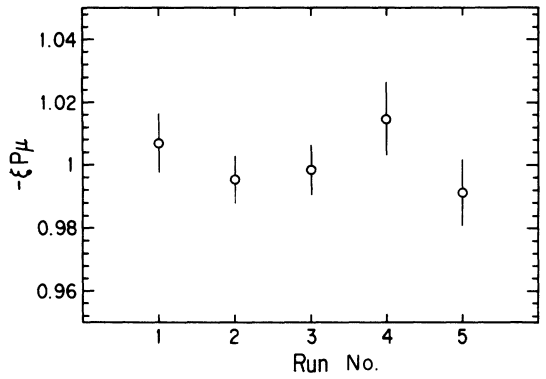

FIG. 18. Results of $-\xi P_\mu$ for run 1-5. They are quite consistent with each other.

particle identification by TOF is negligible. Totally, the correction and error due to muon depolarization became $\delta P = +0.0021 \pm 0.0005$; it was smaller than that due to the positron asymmetry attenuation.

The $A_{\rm obs}$ and their corrected values are listed in Table VIII along with the finally obtained ξP_μ of each run. The values of ξP_μ are also shown in Fig. 18; they are consistent with each other. This fact justifies both the simulation of the positron scattering process and the method of subtracting the π^+ in-flight decay background process.

In order to combine these five runs while considering the error correlation, we defined the weighted average of ξP_μ as

$$\langle \xi P_\mu \rangle = \sum_\alpha \omega_\alpha \xi P_{\mu,\alpha} , \tag{6.1}$$

where α denotes the run number and ω_α is the weight of run α, which are proportional to the number of events of each run. $\xi P_{\mu,\alpha}$ are not independent of each other, since the same corrections were simultaneously applied. In order to separate such dependences for taking an average, the above equation was decomposed as follows:

$$\begin{aligned}
\langle \xi P_\mu \rangle &= \omega_1\{3[A_1 + \delta A^3_{\rm sim} + \delta A_{\rm bg} R^3_{\rm bg}/R_1 + \delta A] + \delta P\} + \omega_2\{3[A_2 + \delta A^5_{\rm sim} + \delta A_{\rm bg} R^5_{\rm bg}/R_{2,3} + \delta A] + \delta P\} \\
&\quad + \omega_3\{3[A_3 + \delta A^A_{\rm sim} + \delta A_{\rm bg} R^5_{\rm bg}/R_{2,3} + \delta A] + \delta P\} + \omega_4\{3[A_4 + \delta A^3_{\rm sim} + \delta A_{\rm bg} R^3_{\rm bg}/R_4 + \delta A] + \delta P\} \\
&\quad + \omega_5\{3[A_5 + \delta A^3_{\rm sim} + \delta A_{\rm bg} R^3_{\rm bg}/R_5 + \delta A] + \delta P\} \\
&= 3\{\omega_1 A_1 + \omega_2 A_2 + \omega_3 A_3 + \omega_4 A_4 + \omega_5 A_5\} && \text{(6.2a)} \\
&\quad + 3\{(\omega_1 + \omega_4 + \omega_5)\delta A^3_{\rm sim} + \omega_2 \delta A^5_{\rm sim} + \omega_3 \delta A^A_{\rm sim}\} && \text{(6.2b)} \\
&\quad + 3\{(\omega_2 + \omega_3) R^5_{\rm bg}/R_{2,3} + (\omega_1/R_1 + \omega_4/R_4 + \omega_5/R_5) R^3_{\rm bg}\}(\tfrac{1}{3} - A_{\rm bg}) && \text{(6.2c)} \\
&\quad + 3\delta A + \delta P , && \text{(6.2d)}
\end{aligned}$$

where superscripts 3, 5 and A, respectively, denote the 3 and 5 mm thick targets and 5 mm with the absorber. The subscripts are either run numbers (1–5) or run conditions (sim is the simulation, bg is the background).

The first term (6.2a) is the sum of the observed asymmetries (A_α), which were clearly independent of each other. The second term (6.2b) is the correction evaluated by a Monte Carlo simulation, which was carried out with respect to the condition of the target thickness and the absorber. Thus, for run 1, 4, and 5, the same simulated value was applied. The third term (6.2c) is the correction due to background contamination. Although the background asymmetry ($A_{\rm bg}$) was the same for all runs, the event rates were estimated with respect to the target thickness and the beam momentum. The other two terms (6.2d) are the other corrections, and were applied simultaneously.

After decomposing the values, the errors of each term were quadratically summed; the final result became

$$\xi P_\mu = -0.9996 \pm 0.0030(\text{stat}) \pm 0.0048(\text{syst}),$$

where the (stat) is the statistical error coming from the first term (6.2a), and (syst) is the systematic error from the other terms.

This result improves the accuracy by an order of magnitude over that of the previous kaon decay experiment [19,20]. It reveals that the V–A hypothesis is still valid for the $K_{\mu 2}$ decay to the 1% level. By summing the statistical and systematic errors quadratically and normalizing the results in the physically significant region ($|\xi P_\mu| < 1$), the present result yields a limit of

$$|\xi P_\mu| > 0.990 \ \ (90\%\ \text{C.L.}) .$$

VII. DISCUSSION

A. Limits on m_{W_2} with massless ν_R

Here, we assume massless neutrinos (including right-handed neutrinos) within nonmanifest LRS models. In the special condition, $\zeta = 0$, which is consistent with the other experiment, such as the ρ parameter measurement [8] at the moment, the present result gives $m_{W_2} > 652$ GeV/c^2 (90% C.L.) for $|\sin\theta_R| = 1$ from Eq. (1.1). The mass limit becomes much lower ($m_{W_2} > 303$ GeV/c^2, 90% C.L.) in the case of $|\sin\theta_R| = 0$. Figure 19 shows the limit from the present experiment together with that from the $\pi_{\mu 2}$ decay experiment performed at TRIUMF [9,10]. By combining both the kaon and pion decay

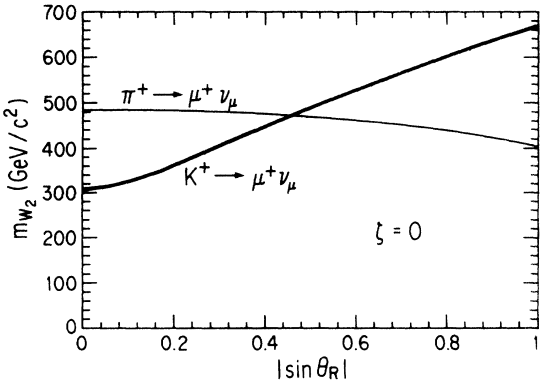

FIG. 19. Limit on m_{W_2} as a function of $|\sin\theta_R|$ from the present result is shown by the thick curve. The limit of the $\pi_{\mu 2}$ decay experiment, which was performed at TRIUMF [9,10], is also shown in the thin curve with the assumption that $\delta = \rho = 3/4$. $\zeta = 0$ is assumed for these curves. The area below the curves is disallowed at the 90% confidence level.

experiments in this figure, the mass limit on the W_2 for an arbitrary θ_R was improved from 404 GeV/c^2 to 468 GeV/c^2 (90% C.L.). The situation at $|\sin\theta_R| \simeq 1$ means that the right-handed current is seen mostly in the $\Delta S = 1$ process, and that the present kaon experiment gives the highest upper limit of m_{W_2}.

In the case of an arbitrary ζ, the constraints of ϵ as a function of ζ are shown in Fig. 20 for $\theta_R = 0$, $\pi/2$, π, and $3\pi/2$ cases. The constraints from the $\pi_{\mu 2}$ decay experiment [9,10], the ρ measurement [8], and the nuclear β-decay experiment [6,7] are also shown in the same figure. The ρ parameter does not suffer from any structure of the hadron vertex and, thus, does not depend on θ_R.

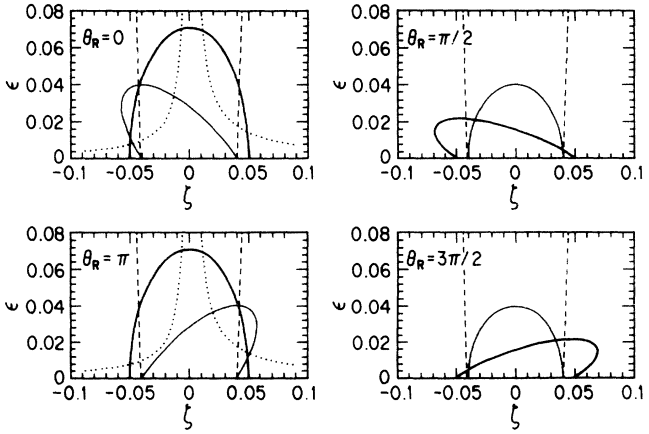

FIG. 20. Limits on ϵ as a function of arbitrary ζ for several cases of θ_R. The thick curves are from the present result. The thin curves are from the $\pi_{\mu 2}$ experiments [9,10]. The dashed and dotted curves are from the ρ measurement [8] and the nuclear β-decay experiment [7,6], respectively. The β-decay experiment gives no limits in the case of $\theta_R = \pi/2$, $3\pi/2$.

In the case of $|\sin\theta_R| \simeq 1$, the constraints derived from nuclear β decay become meaningless. The present experiment excludes a new region around $|\sin\theta_R| \simeq 1$.

B. Limits on m_{W_2} with heavy ν_R

Here, heavy right-handed neutrinos ($m_{\nu_R} \lesssim 80$ MeV/c^2) are considered for both the $K_{\mu 2}$ and $\mu^+ \rightarrow e^+ \nu_e \bar{\nu}_\mu$ decay. For simplicity $\zeta = 0$ is assumed in the following discussion.

The muon polarization is a superposition of the ordinary V–A decay and the $V + A$ decay via heavy ν_R, as

$$P_\mu = \frac{-1 + (\rho_R/\rho_L)(b\epsilon)^2 P_{\nu_R}}{1 + (\rho_R/\rho_L)(b\epsilon)^2}, \tag{7.1}$$

where $b = |\sin\theta_R / \sin\theta_L|$ and $\epsilon = m^2_{W_1}/m^2_{W_2}$. $\rho_{R,L}$ are the kinematic factors for the right-handed and left-handed decays, respectively. P_{ν_R} is the kinematically calculated polarization of the heavy right-handed neutrino, as is described in Appendix C.

The ξ parameter is also affected by the superposition of both ordinary V–A decay and V+A decay accompanied by a heavy ν_R. Thus, ξ becomes

$$\xi = 3\frac{\int C(x)\,dx - \epsilon^2 \int C_H(m_{\nu_R}, x)\,dx}{\int I(x)\,dx + \epsilon^2 \int I_H(m_{\nu_R}, x)\,dx}. \tag{7.2}$$

Here, I_H and C_H are, respectively, the isotropic and cosine terms of the pure V–A muon decay with heavy neutrino emission, which were formulated by Rekalo [46].

With these formula, the limits on m_{W_2} as a function of the ν_R mass were evaluated as shown in Fig. 21. The limits from the measurement of the end-point spectrum

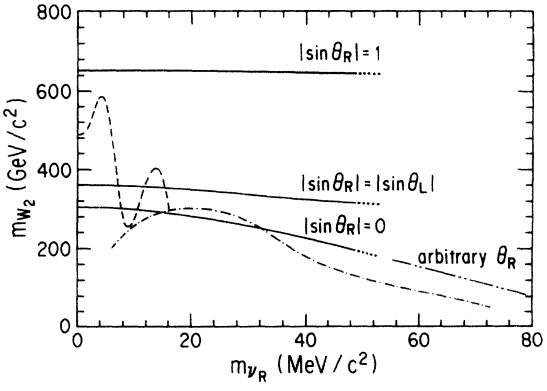

FIG. 21. Limits on m_{W_2} as a function of m_{ν_R}. The bold curve is the limit for maximum $|\sin\theta_R|$, while the other thin solid curves are limits for $|\sin\theta_R| = |\sin\theta_L|$ and $|\sin\theta_R| = 0$. The dot-dot-dashed curve in $m_{\nu_R} > 50$ MeV/c^2 indicates the limit for arbitrary θ_R. The dashed curve [10] and the dot-dashed curve [31] are, respectively, from analyses of the end point asymmetry measurement at TRIUMF.

TABLE IX. 90% confidence level limits on the coupling constants in the HPF representation based on only the present result. Improved new limits are indicated by an asterisk. No limits were put on $|h_{12}|$, $|h_{22}|$ and $|g_{22}|$. Values included in parentheses are limits in Ref. [31].

$\|h_{11}\| < 0.14$ (0.066)	$\|g_{11}\| < 0.07$ (0.033)	
$\|h_{21}\| < 0.14$ (0.125)	$\|g_{21}\| < 0.07$ (0.060)	$\|f_{11}\| < 0.07$ (0.036)
$\|h_{12}\| < \cdots$ (0.424)	$\|g_{12}\| < 0.07^*$ (0.110)	$\|f_{22}\| < 0.04^*$ (0.122)
$\|h_{22}\| < \cdots$ (0.918)	$\|g_{22}\| > \cdots$ (0.888)	

of the decay positron of the $\pi_{\mu 2}$ muon are also indicated in this figure by the dashed and dot-dashed curves [10,31]. The limits obtained from the present experiment weakly depend on m_{ν_R}. In the region $m_{\nu_R} \lesssim 50$ MeV/c^2, three cases ($|\sin\theta_R| = 0$, $|\sin\theta_R| = |\sin\theta_L|$, and $|\sin\theta_R| = 1$) are considered.

In the case of $m_{\nu_R} \gtrsim 50$ MeV/c^2, the decay muon coupled with the ν_R has a lower momentum than the momentum acceptance of the present beam line; P_μ thus definitely equals -1. However, since $V + A$ currents may admix to muon decay, the limit on m_{W_2} becomes as shown in Fig. 21 by the dot-dot-dashed curve.

C. Limits on the Lorentz-covariant coupling constants

In a general four-fermion interaction theory, ξ is

$$1-\xi = \frac{8}{\Gamma_0}\{4(|g_{11}|^2 + 2|g_{12}|^2 - |g_{21}|^2) + |h_{11}|^2 + |h_{21}|^2 - 4|f_{11}|^2 + 16|f_{22}|^2 - 8\mathrm{Re}(h_{11}f_{11}^* - h_{22}f_{22}^*)\}, \quad (7.3)$$

where

$$\Gamma_0 = 4\{4(|g_{22}|^2 + |g_{11}|^2 + |g_{12}|^2 + |g_{21}|^2) + |h_{11}|^2 + |h_{12}|^2 + |h_{21}|^2 + |h_{22}|^2 + 12(|f_{11}|^2 + |f_{22}|^2)\}, \quad (7.4)$$

with the helicity projection form (HPF) representation [47]. The parameter Γ_0 determines the total rate of muon decay. In the case of V–A dominance, $g_{22} \simeq 1$ and the other parameters are small. Thus, in order to obtain approximate limits on the parameters, we assumed $g_{22} = 1$ (the other parameters vanish), and then searched for each limit by scanning each parameter one by one. The limits based on the present experiment are listed in Table IX. Improved limits were obtained for $|g_{12}|$ and $|f_{22}|$. In order to obtain ξ from the present experimental result, $P_\mu = -1$ was assumed. This assumption is partly justified since $|P_\mu| < 1$ makes the limits stringent, except for $|g_{21}|$ and $|f_{11}|$.

ACKNOWLEDGMENTS

We would like to express our thanks to Professor Yoshimitsu Shimizu for discussions concerning the spin flip scattering processes. We are grateful to Professor H. Sugawara, Professor K. Nakai, and Professor S. Iwata for their encouragement and discussions. Thanks are also due to the operating crew of the KEK proton synchrotron and its experimental facilities for their cooperation during the experiment. Some of the authors (M.A. and H.O.) were partially supported by the JSPS.

APPENDIX A: NEUTRINO MASS

Even if the weak interaction occurs via pure V–A currents, the muon polarization would deviate from unity if the neutrino has a finite mass. The following two cases are interesting to us: (i) a mass of ν_μ and (ii) heavy neutrino mixing. In the following discussion we assume pure V–A currents.

1. Mass of ν_μ

In $K_{\mu 2}$ decay with heavy neutrino emission the polarization of the decay muon is given by Eq. (C1). The parameter ξ also changes to

$$\xi_H = 3\frac{\int C_H(m_{\nu_\mu}, x)\,dx}{\int I_H(m_{\nu_\mu}, x)\,dx}, \quad (A1)$$

where C_H and I_H were formulated by Rekalo [46]. Thus, the deviation of ξP_μ from unity may be a signal of the mass of ν_μ. The most stringent limit on m_{ν_μ} was obtained from a precise measurement of the muon momentum in $\pi_{\mu 2}$ decay, and sets $m_{\nu_\mu} < 270\,\mathrm{keV}/c^2$ [48]. This limit corresponds to $\xi_H P_{\mu H} > 0.9999$. Therefore, there is no new constraint on the ν_μ mass from the present limit ($\xi P_\mu > 0.990$), which would indicate only $m_{\nu_\mu} < 4.4$ MeV/c^2.

2. Heavy neutrino mixing

If neutrinos have masses, the muon neutrino would be a superposition of the mass eigenstates of these heavy neutrinos with a mixing matrix, V_{ai}:

$$\nu_\mu = \sum_i V_{\mu i}\nu_i\ ,$$

where the ν_i denotes the mass eigenstates of the neutrinos.

In order to simplify the arguments, only two neutrinos

are considered here: one is the muon neutrino and the other is a heavy neutrino, the candidate of which is limited to ν_τ, since the number of neutrino generations was established to be 3 [49]. The muon polarization via the pure $V-A$ interaction is

$$P_\mu = \frac{-1+\rho|V|^2 P_{\nu_H}}{1+\rho|V|^2}. \quad \text{(A2)}$$

The P_{ν_H} and ρ are, respectively, the muon polarization and a phase-space factor accompanied by heavy neutrino emission.

The effect of heavy neutrino mixing on ξ was calculated by using C_H and I_H, and was combined with the above P_μ. The present experimental limit ($|\xi P_\mu| > 0.990$) gives $|V|^2 < 2.9 \times 10^{-2}$ for the case that $m_{\nu_H} = 35\ \mathrm{MeV}/c^2$, which is a recent limit on the mass of ν_τ [50]; the limit weakens when m_{ν_H} becomes small.

The above limit is weaker than the limit derived from a search for ν_μ-ν_τ oscillation [51], which gives $|V|^2 < 0.013$ for $\Delta m^2 > 100\,\mathrm{eV}^2$, as well as from heavy neutrino search experiments [52,53].

APPENDIX B: MONTE CARLO SIMULATION

In order to estimate the influence of the reaction of the decay positrons in the muon stopping target, we required a precise simulation with an accuracy of $|\delta A| < 0.001$. Since the magnitude of the asymmetry attenuation is ~ 0.01, a simulation accuracy to that attenuation must be several percent for our purpose, and EGS4 is quite sufficient. The quantities which should be precisely estimated were the scattering angle and the multiplicity of knock-on electrons.

For the scattering-angle simulation, large-angle scattering must be taken into account as well as small-angle scattering. This is because the main source of the correction results from the large-angle scattering of positrons. That is, even if a positron initially moves along the target plane, it enters the positron chamber by large-angle scattering. As for the multiplicity of knock-on electrons, the events coinciding with the veto counter hit by these knock-on electrons were rejected in the trigger level. This veto scheme deforms the response function of the positron detector, since the cross section of the knock-on process depends on the primary positron energy.

1. Simulation conditions

In the simulation, we used EGS4 [39], which was originally developed at SLAC for a high-energy electromagnetic-gamma shower simulation. However, it is also applicable below 20 MeV by using a new algorithm with a positron losing a fixed fraction of its energy via a continuous energy loss in a step, which was recommended by Rogers [54] and was employed for the present simulation with 1% of that fixed fraction (ESTEPE $\equiv$ 0.01). Futhermore, the percentage of steps without multiple-scattering processes was kept at 0.35%. With this conditions, EGS4 produces the angular distribution correctly, even at low energy. For example, Rogers reported that the calculated back-scattering coefficient well coincide with the experimental value.

Bhabha scattering is indispensable for estimating the multiplicity of knock-on electrons. Although the cross section was formulated exactly in EGS4, it diverges in the small-angle region, so that the cutoff energy of a recoil electron (A_E) must be set using a numerical calculation. Regarding the Bhabha scattering of which a knock-on electron has a lower energy than A_E (thus, those knock-on electrons are not created in the simulation), the primary positrons were assumed to lose energy via "continuous energy loss" processes without any knock-on electron generation. Since that algorithm makes an overestimation to the energy loss in thin matter, A_E must be sufficiently small compared to the initial energy. In the present calculation, an energy greater than 1 MeV is interesting, so that $A_E - m_e = 10\,\mathrm{keV}$ gives only a 1% overestimation to the energy loss at most, where m_e is the mass of an electron. Thus, we decided to take $A_E = 10\,\mathrm{keV} + m_e$ for the present simulation. Since the same overestimation also occurs in the bremsstrahlung process, the cutoff energy of a produced gamma ray in the bremsstrahlung process (P_E) was also set at 10 keV.

The objects modeled in the present simulation were the muon stopping target, the veto counters (AT, AB, and X), EDC, the e^+ counters, and the aluminum absorbers. The magnetic field was also taken into account.

Other cutoff parameters for charged-particle tracking (ECUT) and for photon tracking (PCUT) were set to ECUT = 0.6 MeV and PCUT = 0.1 MeV, respectively. Particles with an energy smaller than these parameters were treated as being stopped in the current point. The reason why these values were selected is that the detection threshold of the counters was at least $\simeq$ 100 keV. In order to check the validity of these values, a high-threshold simulation was carried out and compared with a normal simulation.

As an initial condition of the simulation, the muon was located in the muon-stopping target with a realistic distribution along the Y and L directions. A uniform distribution was assumed in the T direction. A decay positron was generated with a Michel spectrum, including the radiative corrections (see Appendix D).

2. Ambiguities of the simulation

The ambiguities in the present simulation resulted from two reasons: one was the implementation of physical processes in the EGS4 code; the other was the modeling of the present experimental apparatus. These ambiguities are discussed here in detail. The total systematic error of the Monte Carlo simulation was calculated by summing these components quadratically, and was $\delta A = \pm 0.00073$.

a. Cross-section ambiguity

In the EGS4 simulation the path length between the current point and the next interaction point is calcu-

lated from the cross section at the current positron energy (E_0). However, the interaction cross section at the next point must be estimated using the positron energy at the next point (E), which is smaller than E_0 by the positron energy loss via a continuous energy-loss process. At a higher energy region ($T > 4.5\,\mathrm{MeV}$), the cross section decreases with decreasing energy. Thus, the cross section tends to be overestimated. Since EGS4 is equipped with a novel algorithm to avoid such an overestimation, it causes no difficulty. On the other hand, an underestimation of the cross section will occur in the low-energy region, and EGS4 is defenseless against such an underestimate. This fact was first pointed out by Rogers [54]; the underestimation is about -25% (for Si) *at most*. The magnitude of the underestimation depends on the material type. For aluminum, the cross section is underestimated by -10% at $T < 1\,\mathrm{MeV}$. This underestimation reduces the multiplicity of the knock-on electrons, and generally varies the simulation results.

For primary positrons, this underestimation does not significantly affect the results, since the low-energy contribution is small at first. For knock-on electrons, it changes the multiplicity of the knock-on electrons by -10% for $T < 1\,\mathrm{MeV}$. From a simulation study, the asymmetry of events with low energy ($T < 1\,\mathrm{MeV}$) knock-on electron hitting the veto counter was estimated to be $A = 0.28 \pm 0.01$; the events fraction was 0.01/MeV. Thus, this effect gives a bias of $\delta A = -(1/3 - 0.28) \times 0.01 \times 0.1 = -0.00005$ to the simulated asymmetry. For events triggered by the knock-on electron, the same discussion gives the same value, but with opposite sign. Thus, it is assumed that the cross-section ambiguity gives an asymmetry bias of $|\delta A| < 0.0001$, at most. This value was assigned to the systematic error of the asymmetry correction.

b. Veto geometry

The position of the veto counters in simulation space might differ from the real position of the counters. This is because the veto counter position might have moved by 5 mm (at most) during a data-taking run. This uncertainty might have caused an error in the veto acceptance of 3%. Based on a simulation with an enlarged veto-counter acceptance, we decided to assign $|\delta A| < 0.00009$ to the positron asymmetry uncertainty.

c. Veto threshold

The threshold energy of the veto counters was estimated from the thickness of the material between the muon stopping target and the plastic scintillator of the counter. If the signal-discrimination level is also considered, the threshold energy should be $T_{\mathrm{thre}} < 300\,\mathrm{keV}$. On the other hand, from the simulation study the positron asymmetry of the events with a small energy deposition on the veto counter ($100\,\mathrm{keV} < T < 400\,\mathrm{keV}$) was $A = 0.28 \pm 0.01$, and the events fraction was 0.01/MeV. Thus, the uncertainty of the veto threshold gives only $\delta A < (1/3 - 0.28) \times 0.01 \times 0.3 = 0.0002$ at most.

d. Trigger threshold

The energy threshold of the trigger counter was $T = 930 \pm 150\,\mathrm{keV}$ in the present experiment. This uncertainty does not affect the primary positron asymmetry at all, since the low-energy region of the Michel spectrum is less important. However, it affected the low-energy knock-on electrons, which triggered the detector instead of the primary positrons. The asymmetry of such low-energy knock-on electrons was estimated to be $A = 0.18 \pm 0.01$, and the fraction was $f = 0.007/\mathrm{MeV}$ based on a simulation study. Thus, we assigned $|\delta A| < 0.0002$ to the asymmetry uncertainty coming from the trigger threshold uncertainty.

e. Source distribution

In the simulation muon decay points were distributed realistically along the Y and L directions with the experimentally obtained distribution map. For the T direction, a uniform distribution was assumed, but was, in fact, not uniform.

The target was sliced into several layers, and the source point dependence was estimated. Since the left and right arms compensated each other, the asymmetry did not depend very much on the layer. By comparing the uniform and realistic distributions, the associated uncertainty was estimated to be $|\delta A| < 0.0003$. For the Y and L directions, the position dependence of the asymmetry was also studied by comparing the realistic and uniform distributions; it was found that $|\delta A| < 0.0003$ (Y) and < 0.0005 (L).

APPENDIX C: KINEMATICS OF HEAVY NEUTRINO EMISSION

For $K^-_{\mu 2}$ decay with heavy neutrino emission via V–A currents, the polarization of the decay muon was given by Shrock [55] as

$$P_{\mu^-} = \frac{(\delta_\mu - \delta_\nu)\lambda^{1/2}(1, \delta_\mu, \delta_\nu)}{(\delta_\mu + \delta_\nu) - (\delta_\mu - \delta_\nu)^2}\,, \tag{C1}$$

with

$$\delta_\mu = (m_\mu/m_K)^2, \quad \delta_\nu = (m_\nu/m_K)^2,$$

and

$$\lambda(1, \delta_\mu, \delta_\nu) = 1 + \delta_\mu^2 + \delta_\nu^2 - 2(\delta_\mu + \delta_\nu + \delta_\mu\delta_\nu)\,.$$

Here, λ is proportional to a two-body phase-space factor. We should change the sign of the above original P_μ in order to apply it to the $K^+_{\mu 2}$ decay. For $V + A$ currents we must change the sign again.

The event rate of heavy neutrino emission is proportional to the kinematic rate factor (ρ):

$$\rho(\delta_\mu, \delta_\nu) = f_m(\delta_\mu, \delta_\nu)\lambda^{1/2}(1, \delta_\mu, \delta_\nu), \tag{C2}$$

where $f_m(x,y) = x+y-(x-y)^2$ and denotes the helicity effect.

APPENDIX D: RADIATIVE CORRECTION

In $\mu \to e\nu\bar{\nu}$ decay we should consider the virtual-photon amplitudes of Figs. 22(a)–22(c), in order to pick out information concerning the weak interaction from the observed ξP_μ. Furthermore, if an experiment does not discriminate ordinary muon decay from muon decay accompanied by the emission of a real photon [Figs. 22(d) and 22(e)]

$$\mu \to e\nu\bar{\nu}\gamma,$$

we must also consider this radiative decay process.

The decay spectrum of muons is given, to the order of α, by [40]

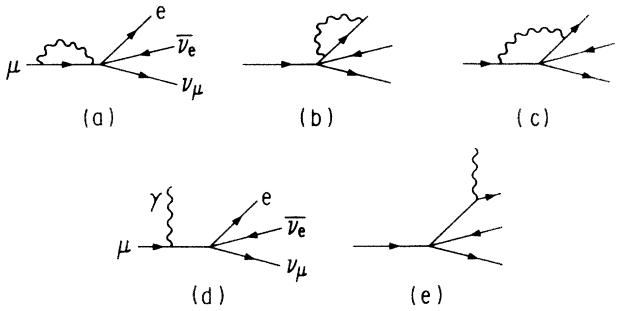

FIG. 22. Lowest-order diagrams of the radiative corrections to muon decay (a–c), and those of radiative muon decay (d,e).

$$\frac{d\Gamma(x,\theta)}{dx\,d\theta} = \frac{1}{2}\Gamma_0\left\{3-2x+\frac{\alpha}{2\pi}f(x) + \xi P_\mu \cos\theta\left[1-2x+\frac{\alpha}{2\pi}g(x)\right]\right\}x^2, \tag{D1}$$

where Γ_0 is the decay constant and

$$f(x) = (6-4x)R(x) + (6-6x)\ln x + \frac{1-x}{3x^2}[(5+17x-34x^2)(w+\ln x) - 22x + 34x^2], \tag{D2}$$

$$g(x) = (2-4x)R(x) + (2-6x)\ln x - \frac{1-x}{3x^2}\left[(1+x+34x^2)(w+\ln x) + 3 - 7x - 32x^2 + \frac{4(1-x)^2}{x}\ln(1-x)\right] \tag{D3}$$

with $w = \ln(m_\mu/m_e) = 5.332$.

In the case of the two-component theory,

$$R(x) = 2\sum_{n=1}^{\infty}\frac{x^n}{n^2} - \frac{1}{3}\pi^2 - 2 + w\left[\frac{3}{2} + 2\ln\left(\frac{1-x}{x}\right)\right] - \ln x(2\ln x - 1) + \left(3\ln x - 1 - \frac{1}{x}\right)\ln(1-x). \tag{D4}$$

Thus, the positron decay asymmetry with the radiative process can be obtained by modifying $I(x)$ and $C(x)$ in Eq. (2.2) to

$$I(x) \to I(x) + \frac{\alpha}{2\pi}x^2 f(x) \tag{D5}$$

and

$$C(x) \to C(x) - \frac{\alpha}{2\pi}x^2 g(x). \tag{D6}$$

The $I(x)$ and $C(x)$ with these corrections are also given in Fig. 2. The radiative correction depends on the positron detection threshold and, thus, will give $\delta A \simeq +0.0009$ for run 1,2,4,5 and $\delta A \simeq +0.0007$ for run 3. We included this correction in the simulation code.

Radiative corrections have also been studied within the framework of intermediate vector bosons. They are those of the four-fermion interaction plus additional terms of the order $\alpha(m_\mu/m_W)^2$ [56]. Since the accuracy goal of the present experiment was about ~ 0.005, the radiative correction estimated in the four-fermion interaction was sufficient.

[1] C. S. Wu *et al.*, Phys. Rev. **105**, 1413 (1957).
[2] R. L. Garwin, L. M. Lederman, and M. Weinrich, Phys. Rev. **105**, 1415 (1957).
[3] J. I. Friedman and V. L. Telegdi, Phys. Rev. **105**, 1681 (1957).
[4] R. P. Feynman and M. Gell-Mann, Phys. Rev. **109**, 193 (1958).
[5] M. Goldhaber, L. Grodzins, and A. W. Sunyar, Phys. Rev. **109**, 1017 (1958).
[6] V. A. Wichers *et al.*, Phys. Rev. Lett. **58**, 1821 (1987).
[7] A. S. Carnoy *et al.*, Phys. Rev. Lett. **65**, 3249 (1990).
[8] S. E. Derenzo, Phys. Rev. **181**, 1854 (1969).

[9] D. P. Stoker *et al.*, Phys. Rev. Lett. **54**, 1887 (1985).
[10] A. Jodidio *et al.*, Phys. Rev. D **34**, 1967 (1986); **37**, 237(E) (1988).
[11] I. Beltrami *et al.*, Phys. Lett. B **194**, 326 (1987).
[12] H. Abramowicz *et al.*, Z. Phys. C **12**, 225 (1982).
[13] G. Beall, M. Bander, and A. Soni, Phys. Rev. Lett. **48**, 848 (1982).
[14] J. Trampetić, Phys. Rev. D **27**, 1565 (1983).
[15] R. N. Mohapatra, G. Senjanović, and M. D. Tran, Phys. Rev. D **28**, 546 (1983).
[16] P. Langacker and S. U. Sankar, Phys. Rev. D **40**, 1569 (1989).
[17] G. Altarelli and P. Franzini, Z. Phys. C **37**, 271 (1988).
[18] L. Michel, Proc. Phys. Soc. **A63**, 514 (1950).
[19] R. S. Hayano *et al.*, Phys. Rev. Lett. **52**, 329 (1984).
[20] T. Yamanaka *et al.*, Phys. Rev. D **34**, 85 (1986).
[21] J. C. Pati, Phys. Rev. D **10**, 275 (1974).
[22] R. N. Mohapatra and J. C. Pati, Phys. Rev. D **11**, 2558 (1975).
[23] N. Cabibbo, Phys. Rev. Lett. **10**, 531 (1963).
[24] M. A. B. Bég *et al.*, Phys. Rev. Lett. **38**, 1252 (1977).
[25] T. Oka, Phys. Rev. Lett. **50**, 1423 (1983).
[26] P. Herczeg, Phys. Rev. **34**, 3449 (1986).
[27] J. Imazato *et al.*, Phys. Rev. Lett. **69**, 877 (1992).
[28] A. E. Pifer, T. Bowen, and K. R. Kendall, Nucl. Instrum. Methods **135**, 39 (1976).
[29] N. K. Abrosimov *et al.*, Pis'ma Zh. Eksp. Teor. Fiz. **36**, 211 (1982) [JETP Lett. **36**, 261 (1982)]; V. P. Koptev *et al.*, Zh. Eksp. Teor. Fiz. **94**, 1 (1988) [Sov. Phys. JETP **67**, 2177 (1988)].
[30] T. D. Lee and C. N. Yang, Phys. Rev. **108**, 1611 (1957).
[31] B. Balke *et al.*, Phys. Rev. D **37**, 587 (1988).
[32] K. H. Tanaka *et al.*, Nucl. Instrum. Methods Phys. Res. Sec. A **316**, 134 (1992).
[33] V. L. Lyuboshits, Yad. Fiz. **31**, 986 (1980) [Sov. J. Nucl. Phys. **31**, 509 (1980)].
[34] J. H. Brewer *et al.*, in *Muon Physics*, edited by Vernon W. Hughes and C. S. Wu (Academic, New York, 1975), Vol. III.
[35] V. G. Grebinnik *et al.*, Pis'ma Zh. Eksp. Teor. Fiz. **27**, 33 (1978) [JETP Lett. **27**, 30 (1978)].
[36] M. Iwasaki, University of Tokyo (private communication).
[37] F. James and M. Roos, CERN D506 MINUIT (1989).
[38] F. James, supplement to CERN D506 MINUIT (1978).
[39] W. R. Nelson, H. Hirayama, and D. W. O. Rogers, Report No. SLAC-0265, 1985 (unpublished).
[40] T. Kinoshita and A. Sirlin, Phys. Rev. **113**, 1652 (1959).
[41] D. G. Fleming, R. J. Mikula, and D. M. Garner, Phys. Rev. A **26**, 2527 (1982).
[42] K. L. Brown and Ch. Iselin, Report No. CERN-74-2, 1974 (unpublished).
[43] G. W. Ford and C. J. Mullin, Phys. Rev. **108**, 477 (1957).
[44] Y. Akiba *et al.*, Phys. Rev. D **32**, 2911 (1985).
[45] D. Yu. Bardin and S. M. Bilenky, Yad. Fiz. **16**, 557 (1972) [Sov. J. Nucl. Phys. **16**, 311 (1973)]. It is worth mentioning that the factor of the first term of Eq. (31) in this reference ($4m_l^2 f_K c/ux^2$) is incorrect. It should be $4m_l^2 f_K^2 c/ux^2$.
[46] A. P. Rekalo, Yad. Fiz. **13**, 1288 (1971) [Sov. J. Nucl. Phys. **13**, 741 (1971)].
[47] K. Mursula and F. Scheck, Nucl. Phys. **B253**, 189 (1985).
[48] R. Abela *et al.*, Phys. Lett. **146B**, 431 (1984).
[49] OPAL Collaboration, M. Z. Akrawy *et al.*, Phys. Lett. B **231**, 530 (1989); OPAL Collaboration, M. Z. Akrawy *et al.*, *ibid.* **235**, 380 (1990).
[50] H. Albrecht *et al.*, Phys. Lett. B **202**, 149 (1988).
[51] N. Ushida *et al.*, Phys. Rev. Lett. **47**, 1694 (1981).
[52] R. Abela *et al.*, Phys. Lett. **105B**, 263 (1981).
[53] R. S. Hayano *et al.*, Phys. Rev. Lett. **49**, 1305 (1982).
[54] D. W. O. Rogers, Nucl. Instrum. Methods Phys. Res. **227**, 535 (1984).
[55] R. E. Shrock, Phys. Lett. **96B**, 159 (1980).
[56] F. Scheck, Phys. Lett. **44**, 187 (1978).

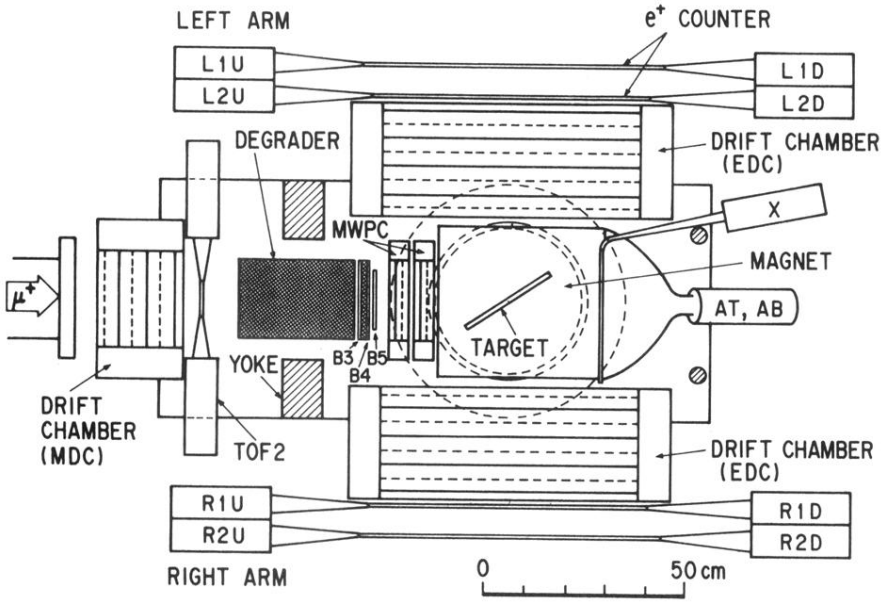

FIG. 4. Top view of the muon polarimeter apparatus. The magnetic field (105 G) at the target is vertical. $B3$, $B4$, and $B5$ are beam-defining counters. AT, AB, and X are veto counters, which are used for detecting muons stopped in the target. EDC's are drift chambers to measure positron emission angle. MDC is a drift chamber used to measure the flight direction of the incident muons. MWPC1/2 are multiwire proportional chambers to measure muon stopping position.